Highlights

A lattice Boltzmann formulation of the one-fluid model for multiphase flow

T. Reis

- A new lattice Boltzmann model for the one-fluid multiphase flow equations
- Surface tension is set precisely *a priori* and independent of other parameters
- Narrow interfaces are captured accurately and efficiently
- Reduced need for on-grid differencing
- Excellent agreement with theoretical and benchmark results

A lattice Boltzmann formulation of the one-fluid model for multiphase flow

T. Reis

School of Computing and Mathematical Sciences, University of Greenwich, London SE10 9LS

Abstract

A multiphase lattice Boltzmann model is constructed to numerically solve the one-fluid flow equations for immiscible fluids. The method features one solver for the macroscopic pressure and momentum and another for a scalar field that captures and sharpens the interface. The surface tension is set *a priori* and independently of other parameters. The interface capillary tensor is embedded within the moments of the lattice Boltzmann equation so that its divergence is captured locally. The algorithm is simple and can compute flows with large density and viscosity ratios while maintaining distributed but narrow interfaces. The model is validated against analytical solutions and benchmark simulations.

Keywords: lattice Boltzmann, multiphase flow, surface tension, one-fluid model

1. Introduction

The lattice Boltzmann method (LBM) for computational fluid dynamics embeds the conservation laws of fluid mechanics into the moments of a velocity-space truncated Boltzmann equation - a linear, constant coefficient hyperbolic system with nonlinear algebraic source terms [1, 2]. This methodology can be extended to multiphase flow, although generally the purely algebraic form of the source terms is sacrificed. LBMs have received particular attention for applications of multiphase flow in porous media and

Email address: T.Reis@greenwich.ac.uk (T. Reis)

microchannels, where surface tension often dominates and spatial resolution may be limited. Indeed, lattice Boltzmann models based on "colour gradient" approaches have been shown to be highly competitive tools for simulating multiphase flow at the pore scale [3, 4].

Surface tension has been incorporated into LBMs using different modelling strategies. Pseudo-potential models, originally proposed by Shan and Chen [5], incorporate surface tension through pair-wise molecular interactions while free-energy models [6] add terms proportional to the density gradient to the equilibrium function to ensure the pressure tensor is related to the multiphase free energy density. A model based on a mean-field approximation for intermolecular attractions was first proposed by He *et al.* [7] and, following important contributions from Wagner [8] on spurious currents in multiphase LBMs, was developed and discretised consistently by Lee and Lin [9] and Lee and Fischer [10]. The model of Lee and Lin [9] includes one discrete velocity Boltzmann equation for pressure (not density) and momentum, and another for the phase field. Slowly varying solutions of the former yield the macroscopic continuity and momentum conservation equations in the incompressible limit and for the latter the Cahn-Hilliard equation with advection. Issues concerning conservation of mass were addressed by Fakhari *et al.* [11] who replaced the Cahn-Hilliard solver with a lattice Boltzmann implementation of the phase field interface tracking equation of Chiu and Lin [12]. Fakhari *et al.* [11] used a multiple relaxation time collision operator to improve numerical stability and adapted a lattice Boltzmann adaptive mesh refinement routine to their multiphase solver. The final algorithm is able to compute complicated multiphase phenomena of practical importance and is more efficient than the previous models of Lee and coworkers that needed to solve a Cahn-Hillard equation with its higher order derivatives.

The original multiphase lattice Boltzmann models of Gunstensen *et al.* [13] and Grunau *et al.* [14] were direct extensions of the Rothman-Keller multiphase lattice gas cellular automaton [15]. Here, distribution functions are labelled with a "colour" to distinguish between fluids and the effect of surface tension is obtained through a perturbation. The coefficient of the perturbation - a controllable parameter - is proportional to the coefficient of surface tension, and a "recolouring" algorithm is applied to maintain narrow phase boundaries. However, the analysis of Reis and Phillips [16] showed that early colour gradient LBMs did not furnish the correct governing equations in the macroscopic limit. In response they redesigned the perturbation to capture the term responsible for interfacial surface tension in the momentum

conservation equation - the interface capillary tensor [17] - and thus showed that colour gradient LBMs can compute solutions to the multiphase Navier-Stokes equations. Colour gradient models with the Reis and Phillips correction have since been extended to three-dimensions and adapted for problems with higher density and viscosity ratios, including flows in microchannels and porous media (see, for example [4, 18, 19, 20, 21, 22] and the references therein). Despite these recent advances and successes, such models are not without their shortcomings: they introduce a spurious viscosity-dependence in the surface tension; the interface between fluids is prone to small scale numerical instabilities and artefacts unless forced to be wider than desired; and they usually require an LBM solver for each phase, which adds unnecessary computational cost and complication. The surface tension defect can be seen in the Chapman-Enskog analysis, and the expression for the "theoretical surface tension" derived in [16, 23], but it is rarely acknowledged. Thus, despite common claims to the contrary, the surface tension cannot be set precisely or consistently *a prior*. Furthermore, attempts to minimise the width of interfaces typically cause them to become fixed to the underlying grid - a spurious phenomenon called lattice pinning [24, 25]. While unrealistically wide interfaces and imprecise surface tension has been a cause for concern for many multiphase LBMs, they are of particular limiting for application where surface tension dominates and mixtures of immiscible fluids propagate thorough tight, perhaps complex, geometries.

Similar to the colour gradient approach, the continuum surface tension chromodynamic model of Lishchuk *et al.* [26, 25] aims to compute solutions to the multiphase Navier-Stokes equations at continuum, hydrodynamic, lengthscales with narrow interfaces. The kinematics of phase separation are not considered to be important at these scales. The surface tension term, which is proportional to the curvature of the interface, is added to the LBM as a direct body force and a recolouring algorithm (usually the one attributed to D'ortona [27]) is needed to segregate fluids. This model has recently been validated and analysed in detail by Speedlove *et al.* [28]. While giving better control over the surface tension and providing a direct route to the continuum surface tension force (CSF) model of Brackbill *et al.* [29], the algorithm needs more finite difference approximations than other colour gradient models. In particular, approximations to second order derivatives are required for the curvature, obtained via the divergence of the interface unit normal vector (other colour models only compute first order gradients). Thus there is an increased computational cost and complexity and an increased risk of grid-

scale instabilities, especially near boundaries. Recolouring is still needed and the challenges of narrowing interfaces and lattice pinning remain. One would prefer, as much as possible, to retain and use the algorithmic advantages of the LBM.

Latva-Kokko and Rothman [24] were the first to study and attempt to quantify lattice pinning in colour gradient models. They identified the recolouring routine as the culprit and suggested an alternative procedure. Their alternative recolouring algorithm, applied to each colour, reduced pinning but at the price of wider interfacial regions. Reis and Dellar [30] provided a detailed theoretical study and explanation of lattice pinning in terms of partial differential equations with stiff source terms for a scalar "phase field" that distinguished between fluids. Their model, which is a lattice Boltzmann implementation of the illustrative problem of LeVeque and Yee [31] but with diffusion, advects the phase field with the flow (which was imposed in this study) and applies a reaction term that counteracts the diffusion and sharpens the interface. Thus the field varies continuously but rapidly across an interface. It is noteworthy that this model is similar in form, although not in formulation, to the sharp phase field tracking equation of Sun and Beckermann [32] for curvature-driven interface motion. Folch *et al.* [33] added a term to Sun and Beckermann's phase field equation to cancel the curvature driven motion, which later Chui and Liu [12] wrote in conservative form. Reis and Dellar [30] showed that excessive sharpening, as determined by the ratio of timescales of the diffusion and reaction terms, causes interfaces to pin to the underlying lattice. They also offered a volume preserving generalisation of the model with random thresholds, as in Bao and Jin [34], that was virtually free from pinning even for extremely narrow interfaces. However, numerical integration was required over to determine global, not local, volume preserving thresholds, making the method difficult to apply for problems with multiple interfaces or breakups. Recently, Reis [35] presented a conservative lattice Boltzmann model for interface advection and sharpening that allowed narrow interfaces to propagate correctly with minimal lattice pinning in stringent tests with significant interface deformation[1]. While it is not feasible in such a formulation to compute vanishingly sharp phase phase boundaries, the interfaces in the test cases in Reis [35] often remained only two or three lattice units wide. The model is based on a single step interpre-

[1]This was originally presented in [36, 37]

tation of the artificial compression algorithm for level set methods of Olsson *et al.* [38], which itself can be viewed as conservative form of the phase field equation of Folch *et al.* [33], as shown by Chui and Liu [12]. Independently, Geier *et al.* [39] formulated an interface tracking equation similar to Chui and Liu [12] as a lattice Boltzmann algorithm which was later used in the multiphase LBM of Fakhari *et al.* [11].

This article proposes a one-fluid lattice Boltzmann model for computing multiphase flow. Like the colour gradient and continuum surface tension chromodynamic models, this new LBM is designed to compute the multiphase Navier-Stokes equations when the lengthscales of phase separation are negligible in comparison to hydrodynamic lengthscales, but to achieve larger density contrasts the modelling is influenced and inspired by the advances of the phase field approaches of Lee and coworkers. One LBM will be used for the hydrodynamic conservation laws and another for capturing the interface. In this one-fluid approach the capillary tensor is embedded directly into the moments of the LBM so that its divergence is captured organically, as inspired by the state-of-the-art in discrete kinetic schemes for magnetohydrodynamics [40], and the interface is captured using the advection-diffusion-sharpening LBM of Reis [35]. However, other interface capturing and sharpening algorithms can could be used in principle. The remainder of the article is organised as follows. In Section 2 we present the governing equations that we wish to solve numerically - the one fluid equations for multiphase flow. In Sections 3 and 4 we present the discrete kinetic formation of the hydrodynamic and interface capturing equations, respectively, and the numerical algorithm is obtained in Section 5. Results are discussed in Section 6 before making concluding remarks in Section 7.

2. Governing equations

The multiphase Navier-Stokes equations with surface tension can be written as [17]

$$\nabla \cdot \mathbf{u} = 0, \tag{1}$$

$$\frac{\partial \rho \mathbf{u}}{\partial t} + \nabla \cdot \rho \mathbf{u}\mathbf{u} = -\nabla P + \nabla \cdot \left(\mu \left(\nabla \mathbf{u} + (\nabla \mathbf{u})^T\right)\right) + \nabla \cdot \left(\sigma \left(\mathbf{I} - \mathbf{n}\mathbf{n}\right) \delta_s\right) + \mathbf{F}. \tag{2}$$

These equations are solved for the fluid velocity, $\mathbf{u}$, and the hydrodynamic pressure, P. Here, $\mathbf{F}$ is an external body force. The third term on the right

hand side of equation (2) is the term responsible for multiphase effects and includes the surface tension, σ, the unit normal to the interface, $\mathbf{n}$, and the surface delta function, δ_s. The surface delta function is the Dirac delta function concentrated on the interface and has the property of converting volume integrals to surface integrals. In principle it can be expressed as $\delta_s(\mathbf{x}) = \delta(n)$, where n is the normal coordinate at the interface and δ is the standard Dirac function, but it requires special treatment in a distributed surface tension numerical model. This is discussed in Section 5. The multiphase term is written as the divergence of the capillary tensor because, conveniently, divergence terms can be naturally incorporated into the moments of a lattice Boltzmann equation without the need for additional finite difference approximations (see Section 3). Still, we note that $\nabla \cdot (\sigma (\mathbf{I} - \mathbf{nn}) \delta_s) = -\sigma\kappa\mathbf{n}\delta_s - \nabla_s\sigma\delta_s$, where $\kappa = \nabla_s \cdot \mathbf{n}$ is the interface curvature and ∇_s is the gradient operator restricted to the interface. The interface may be captured using a scalar field, ϕ, which is assumed to vary smoothly but rapidly between $\phi = 0$ for one fluid and $\phi = 1$ for another across phase boundaries according to

$$\frac{\partial \phi}{\partial t} + \mathbf{u} \cdot \nabla \phi = \kappa \nabla^2 \phi + S(\phi), \tag{3}$$

where κ is a diffusion coefficient and $S(\phi)$ is a sharpening term that helps maintain narrow interfaces. The density, ρ, and dynamic viscosity, μ, in equation (2) may vary between phases and can be computed as functions of ϕ:

$$\rho = \phi\rho_1 + (1-\phi)\rho_2, \tag{4}$$
$$\mu = \phi\mu_1 + (1-\phi)\mu_2, \tag{5}$$

where ρ_1 and ρ_2 are the constant densities of the two fluids, and similarly for μ_1 and μ_2. The unit normal at the interface, which appears in the capillary tensor in the momentum equation (2), can be found according to

$$\mathbf{n} = \frac{\nabla \phi}{|\nabla \phi|}. \tag{6}$$

Equations (1,2,3) are the equations solved in the whole-domain, or "one-fluid" approach to multiphase computational fluid dynamics. In this article we use for the interface sharpening term [35, 38]

$$S(\phi) = -\kappa \nabla \cdot \frac{\phi(1-\phi)}{\lambda} \mathbf{n}, \tag{7}$$

where λ is the sharpening parameter. We note that Reis and Dellar used a purely algebraic sharpening term to capture interfaces, where $S(\phi) \propto \phi(1-\phi)(\phi_c - \phi)$, $\phi_c \in \mathbb{R}$ [30].

3. Discrete velocity Boltzmann formulation of the hydrodynamic equations

We will embed the multiphase Navier-Stokes equations (1,2) into a larger system of PDEs (the moments of a discrete velocity Boltzmann equation), but one that is easier to solve numerically. The discrete velocity Boltzmann equation for f_i, $i = 0, \dots b$, is

$$\frac{\partial f_i}{\partial t} + \mathbf{c}_i \cdot \nabla f_i = -\frac{1}{\tau_f}\left(f_i - f_i^{(0)}\right) + R_i + S_i, \tag{8}$$

where the left-hand side describes the advection of each f_i with corresponding discrete particle velocity $\mathbf{c}_i$ and the first term on the right models the relaxation of f_i to their equilibria $f_i^{(0)}$ over a timescale τ_f. The additional source terms R_i will account for any body forces and S_i will help us recover the continuity equation (discussed below). The discrete particle velocity set, $\{\mathbf{c}_i : i = 0, \dots b\}$ form a lattice, such as the D2Q9 lattice shown in Figure 1 which is used exclusively here. For ease of presentation the model is constructed using a single relaxation time collision on the right hand side of equation (8) but it is applicable to other collision operators. In Section 5 the model is implemented using two relaxation times.

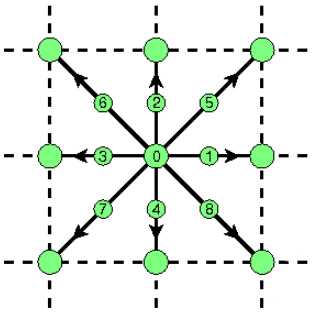

Figure 1: The D2Q9 lattice

Similar to He and Luo [1] and Lee and Lin [9] we define the conserved

moments for pressure and momentum

$$\sum_i f_i = \sum_i f_i^{(0)} = \frac{P}{c_s^2}, \tag{9}$$

$$\sum_i f_i \mathbf{c}_i = \sum_i f_i^{(0)} \mathbf{c}_i = \rho \mathbf{u}, \tag{10}$$

where $c_s = 1/\sqrt{3}$ is the (constant) sound speed. The density of the fluid will be given according to equation (4) and a discrete Boltzmann equation for the scalar field ϕ will be discussed in the Section 4. Since R_i is responsible for a body force it must satisfy the constraints [41]

$$\sum_i R_i = 0, \quad \sum_i R_i \mathbf{c}_i = \mathbf{F}, \quad \sum_i R_i \mathbf{c}_i \mathbf{c}_1 = \mathbf{F}\mathbf{u} + \mathbf{u}\mathbf{F}, \tag{11}$$

where $\mathbf{F}$ is the force. Thus a suitable R_i is

$$R_i = W_i \left(\frac{\mathbf{c}_i - \mathbf{u}}{c_s^2} + \frac{\mathbf{c}_i \cdot \mathbf{u}}{c_s^4} \mathbf{c}_i \right) \cdot \mathbf{F}, \tag{12}$$

where $W_0 = 4/9$, $W_{1,\ldots,4} = 1/9$, and $W_{5,\ldots,8} = 1/36$ are the standard D2Q9 weights.

Taking the first discrete velocity moment of equation (8) yields

$$\frac{1}{c_s^2} \frac{\partial P}{\partial t} + \nabla \cdot (\rho \mathbf{u}) = \frac{1}{c_s^2} \frac{\partial P}{\partial t} + \rho \nabla \cdot \mathbf{u} + \mathbf{u} \cdot \nabla \rho = \sum_i S_i. \tag{13}$$

Following Lee and Lin [9] we remove gradients of density to ensure mass conservation and reduce compressibility errors by requiring

$$\sum_i S_i = \mathbf{u} \cdot \nabla \rho, \tag{14}$$

which yields

$$\frac{1}{\rho c_s^2} \frac{\partial P}{\partial t} + \nabla \cdot \mathbf{u} = 0. \tag{15}$$

Equation (15) resembles an artificial compressibility equation and for low Mach numbers, $Ma = |\mathbf{u}|/c_s \ll 1$, the velocity is approximately divergence free.

Taking the second moment of equation (8) yields the momentum equation

$$\frac{\partial \rho \mathbf{u}}{\partial t} + \nabla \cdot \mathbf{\Pi} = \mathbf{F} + \sum_i S_i \mathbf{c}_i, \tag{16}$$

where the momentum flux tensor $\mathbf{\Pi} = \sum_i f_i \mathbf{c}_i \mathbf{c}_i$. To conserve momentum we ask $\sum_i S_i \mathbf{c}_i = 0$. The momentum flux tensor evolves according to its own PDE, found by taking the third moment of equation (8):

$$\frac{\partial \mathbf{\Pi}}{\partial t} + \nabla \cdot \mathbf{Q} = -\frac{1}{\tau_f}\left(\mathbf{\Pi} - \mathbf{\Pi}^{(0)}\right) + \mathbf{F}\mathbf{u} + \mathbf{u}\mathbf{F} + \sum_i S_i \mathbf{c}_i \mathbf{c}_i, \tag{17}$$

where $\mathbf{\Pi}^{(0)} = \sum_i f_i^{(0)} \mathbf{c}_i \mathbf{c}_i$ and $\mathbf{Q} = \sum_i f_i \mathbf{c}_i \mathbf{c}_i \mathbf{c}_i$.

To find an expression for $\mathbf{\Pi}$ and hence a closed momentum equation we expand the temporal derivatives and non–conserved moments in the PDE system (15,16,17) as

$$\frac{\partial}{\partial t} = \frac{\partial}{\partial t_0} + \tau_f \frac{\partial}{\partial t_1} + \ldots, \quad \mathbf{\Pi} = \mathbf{\Pi}^{(0)} + \tau_f \mathbf{\Pi}^{(1)} + \ldots, \quad \mathbf{Q} = \mathbf{Q}^{(0)} + \tau_f \mathbf{Q}^{(1)} + \ldots, \tag{18}$$

which at leading order gives the closed PDE system

$$\frac{1}{\rho c_s^2}\frac{\partial P}{\partial t_0} + \nabla \cdot \mathbf{u} = 0, \tag{19}$$

$$\frac{\partial \rho \mathbf{u}}{\partial t_0} + \nabla \cdot \mathbf{\Pi}^{(0)} = \mathbf{F}, \tag{20}$$

$$\frac{\partial \mathbf{\Pi}^{(0)}}{\partial t_0} + \nabla \cdot \mathbf{Q}^{(0)} = -\mathbf{\Pi}^{(1)} + \mathbf{F}\mathbf{u} + \mathbf{u}\mathbf{F} + \sum_i S_i \mathbf{c}_i \mathbf{c}_i, \tag{21}$$

where $\mathbf{Q}^{(0)} = \sum_i f_i^{(0)} \mathbf{c}_i \mathbf{c}_i \mathbf{c}_i$. Once we have specified $\mathbf{\Pi}^{(0)}$, which amounts to supplying the equilibria $f_i^{(0)}$, we can find an expression for the first correction, $\mathbf{\Pi}^{(1)}$, to the tensor $\mathbf{\Pi}$. To obtain the one-fluid multiphase Navier-Stokes equations we impose the equilibrium moment

$$\mathbf{\Pi}^{(0)} = P\mathbf{I} + \rho \mathbf{u}\mathbf{u} - \sigma\left(\boldsymbol{I} - \mathbf{n}\mathbf{n}\right)\delta_s. \tag{22}$$

The last term on the right hand side of equation (22) is the capillary tensor responsible for surface tension, as defined in Section 2. An equilibrium

function that satisfies the conservation constraints (9,10) and condition (22) is

$$f_i^{(0)} = W_i \left(\frac{P}{c_s^2} + \frac{\rho \mathbf{u} \cdot \mathbf{c}_i}{c_s^2} + \frac{1}{2c_s^4} \left(\rho \mathbf{u}\mathbf{u} + \boldsymbol{T} \right) : \left(\mathbf{c}_i \mathbf{c}_i - c_s^2 \mathbf{I} \right) \right), \tag{23}$$

where $\boldsymbol{T} = \sigma \left(\boldsymbol{I} - \mathbf{n}\mathbf{n} \right) \delta_s$ is the capillary tensor.

The first term of the left hand side of equation (21) can be written as

$$\partial_{t_0} \boldsymbol{\Pi}^{(0)} = \partial_{t_0} \left(P\mathbf{I} + \rho \mathbf{u}\mathbf{u} - \sigma \left(\mathbf{I} - \mathbf{n}\mathbf{n} \right) \delta_s \right) \tag{24}$$

and we use lower order moment equations to evaluate the temporal derivatives in terms of spatial derivatives. Thus, from equation (19),

$$\partial_{t_0} P = -\rho c_s^2 \nabla \cdot \mathbf{u}, \tag{25}$$

and using equation (20),

$$\begin{aligned} \partial_{t_0} \rho \mathbf{u}\mathbf{u} &= \mathbf{u} \partial_{t_0} \rho \mathbf{u} + \left(\partial_{t_0} \rho \mathbf{u} \right) \mathbf{u} - \mathbf{u}\mathbf{u} \partial_{t_0} \rho, \\ &= -\mathbf{u} \nabla \cdot \boldsymbol{\Pi}^{(0)} + \mathbf{u}\mathbf{F} - \left(\nabla \cdot \boldsymbol{\Pi}^{(0)} \right) \mathbf{u} + \mathbf{F}\mathbf{u} - \mathbf{u}\mathbf{u} \partial_{t_0} \rho, \\ &= -\mathbf{u} \nabla P - (\nabla P)\mathbf{u} + \mathbf{u}\mathbf{F} + \mathbf{F}\mathbf{u} \\ &\quad + \mathbf{u} \nabla \cdot \left[\sigma \left(\mathbf{I} - \mathbf{n}\mathbf{n} \right) \delta_s \right] + \nabla \cdot \left[\sigma \left(\mathbf{I} - \mathbf{n}\mathbf{n} \right) \delta_s \right] \mathbf{u} + \mathcal{O}(\mathrm{Ma}^3). \end{aligned} \tag{26}$$

Inserting equations (25) and (26) into equation (24) shows us that the temporal derivative of the equilibrium part of the momentum flux tensor can be expressed as

$$\begin{aligned} \partial_{t_0} \boldsymbol{\Pi}^{(0)} &= -\rho c_s^2 \mathbf{I} \nabla \cdot \mathbf{u} - \mathbf{u} \nabla P - (\nabla P)\mathbf{u} \\ &\quad + \mathbf{u} \nabla \cdot \left[\sigma \left(\mathbf{I} - \mathbf{n}\mathbf{n} \right) \delta_s \right] + \nabla \cdot \left[\sigma \left(\mathbf{I} - \mathbf{n}\mathbf{n} \right) \delta_s \right] \mathbf{u} \\ &\quad - \partial_{t_0} \left[\sigma \left(\mathbf{I} - \mathbf{n}\mathbf{n} \right) \delta_s \right] + \mathbf{u}\mathbf{F} + \mathbf{F}\mathbf{u} + \mathcal{O}(\mathrm{Ma}^3). \end{aligned} \tag{27}$$

With the equilibrium function supplied, the divergence of the third order tensor in equation (21) is expressed as

$$\nabla \cdot \mathbf{Q}^{(0)} = c_s^2 \nabla \cdot (\rho \mathbf{u}) \mathbf{I} + \rho c_s^2 \left(\nabla \mathbf{u} + (\nabla \mathbf{u})^T \right) + c_s^2 \left(\mathbf{u} \nabla \rho + (\nabla \rho) \mathbf{u} \right). \tag{28}$$

Now substituting this along with equation (27) into equation (21) gives an expression for the first order correction in the expansion of the momentum flux:

$$\begin{aligned} \boldsymbol{\Pi}^{(1)} &= \rho c_s^2 \mathbf{I} \nabla \cdot \mathbf{u} + \mathbf{u} \nabla P + (\nabla P)\mathbf{u} - \mathbf{u} \nabla \cdot \left[\sigma \left(\mathbf{I} - \mathbf{n}\mathbf{n} \right) \delta_s \right] \\ &\quad - \nabla \cdot \left[\sigma \left(\mathbf{I} - \mathbf{n}\mathbf{n} \right) \delta_s \right] \mathbf{u} + \partial_{t_0} \left[\sigma \left(\mathbf{I} - \mathbf{n}\mathbf{n} \right) \delta_s \right] - c_s^2 \mathbf{I} \nabla \cdot (\rho \mathbf{u}) \\ &\quad - \rho c_s^2 \left(\nabla \mathbf{u} + (\nabla \mathbf{u})^T \right) - c_s^2 \left(\mathbf{u} \nabla \rho + (\nabla \rho) \mathbf{u} \right) \\ &\quad + \sum_i S_i \mathbf{c}_i \mathbf{c}_i + \mathcal{O}(\mathrm{Ma}^3). \end{aligned} \tag{29}$$

Noting that $\nabla\cdot(\rho\mathbf{u}) = \rho\nabla\cdot\mathbf{u}+\mathbf{u}\cdot\nabla\mathbf{u}$, the density gradient terms that are in (29) but not in the momentum equation (2) can be removed if $\sum_i S_i\mathbf{c}_i\mathbf{c}_i = c_s^2\left(\mathbf{u}\cdot\nabla\rho\mathbf{I}+\mathbf{u}\nabla\rho+(\nabla\rho)\mathbf{u}\right)$. Following Lee and Lin [9] we define the source term

$$\begin{aligned} S_i &= (\Gamma_i - W_i)(\mathbf{c}_i-\mathbf{u})\cdot\nabla\rho, \\ \Gamma_i &= W_i\left(1+\frac{\mathbf{c}_i\cdot\mathbf{u}}{c_s^2}+\frac{(\mathbf{c}_i\mathbf{c}_i-c_s^2\mathbf{I}):\mathbf{u}\mathbf{u}}{2c_s^4}\right). \end{aligned} \tag{30}$$

This satisfies the previous conditions on the first two moments of S_i and also $\sum_i S_i\mathbf{c}_i\mathbf{c}_i = c_s^2\left(\mathbf{u}\cdot\nabla\rho\mathbf{I}+\mathbf{u}\nabla\rho+(\nabla\rho)\mathbf{u}\right)+\mathcal{O}(\mathrm{Ma}^3)$. Thus the expression for $\mathbf{\Pi}^{(1)}$ simplifies to

$$\begin{aligned} \mathbf{\Pi}^{(1)} &= -\rho c_s^2\left(\nabla\mathbf{u}+(\nabla\mathbf{u})^T\right)+\mathbf{u}\nabla P+(\nabla P)\mathbf{u}-\mathbf{u}\nabla\cdot\left[\sigma(\mathbf{I}-\mathbf{nn})\delta_s\right] \\ &\quad -\nabla\cdot\left[\sigma(\mathbf{I}-\mathbf{nn})\delta_s\right]\mathbf{u}+\partial_{t_0}\left[\sigma(\mathbf{I}-\mathbf{nn})\delta_s\right]+\mathcal{O}(\mathrm{Ma}^3). \end{aligned} \tag{31}$$

Recall from (18) that $\mathbf{\Pi} = \mathbf{\Pi}^{(0)}+\tau_f\mathbf{\Pi}^{(1)}+\mathcal{O}(\tau_f^2)$ so that from the momentum conservation equation (16) we have to first order in τ_f

$$\begin{aligned} \frac{\partial\rho\mathbf{u}}{\partial t}+\nabla\cdot\rho\mathbf{u}\mathbf{u} &= -\nabla P+\nabla\cdot\left(\mu\left(\nabla\mathbf{u}+(\nabla\mathbf{u})^T\right)\right)+\nabla\cdot\left(\sigma(\mathbf{I}-\mathbf{nn})\delta_s\right) \\ &\quad -\nabla\cdot\left(\tau_f\left[\mathbf{u}\nabla P+(\nabla P)\mathbf{u}-\mathbf{u}\nabla\cdot\left[\sigma(\mathbf{I}-\mathbf{nn})\delta_s\right]\right.\right. \\ &\quad \left.\left.-\left[\sigma(\mathbf{I}-\mathbf{nn})\delta_s\right]\mathbf{u}\right]+\tau_f\partial_{t_0}\nabla\cdot\left[\sigma(\mathbf{I}-\mathbf{nn})\delta_s\right]\right)+\mathbf{F} \end{aligned} \tag{32}$$

where $\mu = \rho c_s^2\tau_f$ is the (dynamic) viscosity.

In the standard lattice Boltzmann model for the single phase Navier-Stokes equations, $P = \rho c_s^2$, and the $\mathbf{u}\nabla P$ terms in equation (32) cancel with density gradients that are removed in the current model by the moments of S_i. However, the residual $\mathbf{u}\nabla P$ terms here are of order $\mathcal{O}(\mathrm{Ma}^3)$ and thus can be neglected. The third term on the right hand side of equation (32) is the surface tension term, written as the divergence of the capillary tensor. The other terms involving σ are error surface tension terms that multiply the divergence of the capillary tensor by a term of the order $\mathcal{O}(\mathrm{Ma}^2/\mathrm{Re})$, where $\mathrm{Re} = \rho UL/\mu$ is the Reynolds number and the Mach number, Ma, has already been defined. Thus the error terms are $\mathrm{Re}/\mathrm{Ma}^2$ times smaller than the divergence of the capillary tensor and can safely be neglected. It should also be noted that additional or a change in errors can occur if τ_f varies across an interface, as it may when there are large viscosity contrasts, especially as gradients of the order parameter are approximated numerically

(see Section 5). We concluded that our discrete Boltzmann equation (8) with equilibria (23) has embedded within its moment system the multiphase partial differential equations

$$\frac{1}{\rho c_s^2}\frac{\partial P}{\partial t} + \nabla \cdot \mathbf{u} = 0, \tag{33}$$

$$\begin{aligned}\frac{\partial \rho \mathbf{u}}{\partial t} + \nabla \cdot \rho \mathbf{u}\mathbf{u} &= -\nabla P + \nabla \cdot \left(\mu\left(\nabla \mathbf{u} + (\nabla \mathbf{u})^T\right)\right) \\ &\quad + \nabla \cdot \left(\sigma\left(\mathbf{I} - \mathbf{n}\mathbf{n}\right)\delta_s\right) + \mathbf{F}\end{aligned} \tag{34}$$

4. Discrete velocity Boltzmann formulation of the interface capturing equation

We briefly describe the lattice Boltzmann model of Reis [35, 37] for the advection and sharpening of the scalar field $0 \leq \phi \leq 1$ for capturing interfaces and distinguishing between fluids. The target PDE

$$\frac{\partial \phi}{\partial t} + \mathbf{u} \cdot \nabla \phi = \kappa \left(\nabla^2 \phi - \nabla \cdot \frac{\phi(1-\phi)}{\lambda}\mathbf{n}\right) \tag{35}$$

is embedded into the moments of the discrete Boltzmann equation

$$\frac{\partial g_i}{\partial t} + \mathbf{c}_i \cdot \nabla g_i = -\frac{1}{\tau_g}\left(g_i - g_i^{(0)}\right) + H_i, \quad i = 0, \ldots, d \tag{36}$$

by defining the conserved quantity ϕ to be the first moment of g_i,

$$\phi = \sum_i g_i = \sum_i g_i^{(0)}, \tag{37}$$

and the equilibria and lattice sharpening term

$$g_i^{(0)} = \omega_i \left(\phi + \frac{\mathbf{c}_i \cdot \phi \mathbf{u}}{c_s^2}\right), \tag{38}$$

$$H_i = \frac{\phi(1-\phi)}{\lambda}\mathbf{c}_i \cdot \mathbf{n}. \tag{39}$$

The H_i defined in equation (39) is the compression term that counteracts diffusion and helps to maintain narrow phase transition areas by keeping ϕ close to 1 or 0. In this work we use the D2Q5 discrete velocity set $\{\mathbf{c}_i : i =$

$0, \ldots, 4\}$ for g_i, which can be visualised as the lattice in Figure 1 without the diagonal velocities. The D2Q5 weights are $\omega_0 = 1/3$ and $\omega_{1,\ldots,4} = 1/6$, and $c_s^2 = 1/3$.

Taking moments of equation (36) yields the PDE system

$$\frac{\partial \phi}{\partial t} + \nabla \cdot \boldsymbol{\psi} = 0 \tag{40}$$

$$\frac{\partial \boldsymbol{\psi}}{\partial t} + \nabla \cdot \boldsymbol{\pi} = -\frac{1}{\tau_g}\left(\boldsymbol{\psi} - \boldsymbol{\psi}^{(0)}\right) + c_s^2 \frac{\phi(1-\phi)}{\lambda}\mathbf{n}, \tag{41}$$

where

$$\boldsymbol{\psi} = \sum_i g_i \mathbf{c}_i, \quad \boldsymbol{\psi}^{(0)} = \sum_i g_i^{(0)} \mathbf{c}_i = \phi \mathbf{u}, \quad \boldsymbol{\pi} = \sum_i g_i \mathbf{c}_i \mathbf{c}_i. \tag{42}$$

Following a Chapman-Enskog expansion similar to that in Section 3 and [35] that expands the temporal derivatives and non-conserved moments $\boldsymbol{\psi}$ and $\boldsymbol{\pi}$ in the system (40,41) yields to second order in Mach number the target equation (35) with diffusion coefficient $\kappa = \tau_g c_s^2$.

5. Lattice Boltzmann implementation

Now that we have build discrete velocity Boltzmann PDEs that contain within their moment systems the one-fluid multiphase flow equations (1,2,3), we seek fully discrete algorithms to solve them numerically. To enhance numerical performance we take a two-relaxation-time (TRT) approach which relaxes the symmetric and anti-symmetric moments at different rates [42]. That is, we define

$$\chi_i^{\pm} = \frac{1}{2}\left(\chi_i \pm \chi_j\right),$$

where j is in the opposite direction of i such that $\mathbf{c}_i = -\mathbf{c}_j$, and $\chi_i \in \left\{f_i, f_i^{(0)}, R_i, S_i, g_i, g_i^{(0)}\right\}$.

Let's consider the lattice Boltzmann equation for f_i (and thus hydrodynamic momentum and pressure) first. For simplicity we define the new equilibria

$$f^{(e+)} = f^{(0+)} + \tau_f^+\left(R_i^+ + S_i^+\right), \tag{43}$$

$$f^{(e-)} = f^{(0-)} + \tau_f^-\left(R_i^- + S_i^-\right), \tag{44}$$

where τ_f^+ and τ_f^- are the relaxation times for the symmetric and antisymmetric parts of f_i, respectively, and τ_f^+ controls the viscosity according to

$\mu = \rho c_s^2 \tau_f^+$. Note that if the relaxation times are equal, $\tau_f^+ = \tau_f^- = \tau$, then we have the single relaxation time model. Splitting the collision operator does not effect the model discussed and derived in Section 3.

The TRT discrete velocity Boltzmann equation may now be written as [43]

$$\frac{\partial f_i}{\partial t} + \mathbf{c}_i \cdot \nabla f_i = -\frac{1}{\tau_f^+}\left(f_i^+ - f_i^{(e+)}\right) - \frac{1}{\tau_f^-}\left(f_i^- - f_i^{(e-)}\right) \tag{45}$$

and integrated over a characteristic for time to yield

$$f_i\left(\mathbf{x} + \mathbf{c}_i\Delta t, t + \Delta t\right) - f_i\left(\mathbf{x}, t\right) = \frac{\Delta t}{2}\left(\Omega_i\left(\mathbf{x} + \mathbf{c}_i\Delta t, t + \Delta t\right) + \Omega_i(\mathbf{x}, t)\right) + \mathcal{O}(\Delta t^3), \tag{46}$$

where Ω represents the entire right and side of equation (45). The left hand side of equation (46) is exactly the integral of the left hand side of (45) over a timestep Δt and the trapezium rule has been used to approximate the integral of the right hand side of equation (46) over a timestep.

Equation (46) defines a second order accurate but implicit system of algebraic equations since the terms on the right evaluated at the new time $t + \Delta t$ require hydrodynamic moments of f_i at $t + \Delta t$. For an explicit in time algorithm we introduce the change of variables [44, 45]

$$\overline{f}_i = f_i - \frac{\Delta t}{2}\Omega_i = f_i + \frac{\Delta t}{2\tau_f^+}\left(f_i^+ - f_i^{(e^+)}\right) + \frac{\Delta t}{2\tau_f^-}\left(f_i^- - f_i^{(e^-)}\right) \tag{47}$$

which yields the lattice Boltzmanm equation for $\overline{f}_i$,

$$\begin{aligned}\overline{f}_i\left(\mathbf{x} + \mathbf{c}_i\Delta t, t + \Delta t\right) - \overline{f}_i\left(\mathbf{x}, t\right) = &-\frac{\Delta t}{\tau_f^+ + \Delta t/2}\left(\overline{f}_i^+\left(\mathbf{x}, t\right) - f_i^{(e+)}\left(\mathbf{x}, t\right)\right) \\ &-\frac{\Delta t}{\tau_f^- + \Delta t/2}\left(\overline{f}_i^-\left(\mathbf{x}, t\right) - f_i^{(e-)}\left(\mathbf{x}, t\right)\right),\end{aligned} \tag{48}$$

where $\overline{f}_i^{(\pm)} = \frac{1}{2}\left(\overline{f}_i \pm \overline{f}_j\right)$. Again note that if the relaxation times are equal then the single relaxation time LBE is obtained. The hydrodynamic moments of the transformed variable $\overline{f}_i$ that are needed for the equilibria are

$$\sum_i \overline{f}_i = \frac{P}{c_s^2} - \frac{\Delta t}{2}\mathbf{u} \cdot \nabla\rho, \tag{49}$$

$$\sum_i \overline{f}_i \mathbf{c}_i = \rho\mathbf{u} + \frac{\Delta t}{2}\mathbf{F}. \tag{50}$$

Similarly, the TRT extension of the discrete velocity Boltzmann PDE for g_i is

$$\frac{\partial g_i}{\partial t} + \mathbf{c}_i \cdot \nabla g_i = -\frac{1}{\tau_g^+}\left(g_i^+ - g_i^{(e+)}\right) - \frac{1}{\tau_g^-}\left(g_i^- - g_i^{(e-)}\right), \tag{51}$$

where we have defined

$$g^{(e-)} \;=\; g^{(0-)} + \tau_g^- H_i, \tag{52}$$

noting that there is no symmetric contribution to H_i. The relaxation time τ_g^- sets the diffusion coefficient according to $\kappa = \tau_g^- c_s^2$, and τ_g^+ is chosen on the basis of numerical stability. Following the same discretisation method of integrating over a characteristic for time and applying the trapezium rule, as discussed above, we obtain the lattice Boltzmann equation for g_i [35],

$$\begin{aligned} \overline{g}_i(\mathbf{x}+\mathbf{c}_i, t+\Delta t) - \overline{g}_i(\mathbf{x},t) \;&=\; -\frac{\Delta t}{\tau_g^+ + \Delta t/2}\left(\overline{g}_i^+ - g_i^{(e+)}\right) \\ &-\; \frac{\Delta t}{\tau_g^- + \Delta t/2}\left(\overline{g}_i^- - g_i^{(e-)}\right) \end{aligned} \tag{53}$$

where

$$\overline{g}_i = g_i + \frac{\Delta t}{2\tau_g^+}\left(\overline{g}_i^+ - g_i^{(0^+)}\right) + \frac{\Delta t}{2\tau_g^-}\left(\overline{g}_i^- - g_i^{(e^-)}\right) \tag{54}$$

and $\overline{g}_i^{(\pm)} = \frac{1}{2}\left(\overline{g}_i \pm \overline{g}_j\right)$. Since the scalar field is conserved, $\phi = \sum_i g_i = \sum_i \overline{g}_i$. Clearly, this TRT scheme reduces to the standard single relaxation time approach when $\tau_g^+ = \tau_g^-$.

The gradients that appear in the algorithm (specifically, in S_i and the equilibria for f_i and g_i) are computed using central differencing,

$$\nabla\Theta = \frac{\sum_i \mathbf{c}_i W_i \left[\Theta(\mathbf{x}+\mathbf{c}_i\Delta t) - \Theta(\mathbf{x}-\mathbf{c}_i\Delta t)\right]}{2\Delta t c_s^2}. \tag{55}$$

Note that $\nabla\rho = (\rho_1 - \rho_2)\nabla\phi$. The capillary tensor, $\mathbf{T}$, that appears in the equilibria (23) needs the surface delta function, δ_S, which in this work is approximated by

$$\delta_S \simeq |\nabla\phi|. \tag{56}$$

We note that other approximations are available and the optimal choice is not clear [46, 47]. The definition above has proved to be suitable but it may be improved. The capillary tensor and terms involving $\mathbf{n}$ are computed

whenever $|\nabla\phi| > 0$. The relaxation times τ_f^- and τ_g^+ are set by the products $\Lambda_f = \tau_f^+\tau_f^- = \Lambda_g = \tau_g^+\tau_g^- = 1/4$. This choice of so-called "magic parameter" eliminates the recurrence in non-conserved moments, removes the viscosity dependence in the errors, and offers optimal stability for single phase flow [48, 42, 43]. A summary of the model is algorithm is provided in Appendix A.

6. Results

We run a series of benchmark tests to verify our multiphase model. Unless otherwise stated we set $c = \Delta x/\Delta t = 10$, so that a characteristic length L is broken up into $L/\Delta x$ segments and a characteristic velocity U is scaled so that $U/c \ll 1$ (noting that in so-called lattice units the scaling is such that $\Delta x = \Delta t = 1$ and $U \ll 1$). The reference pressure is set to be $P_0 = 1$, and the reference density $\rho_0 = 1$. Also, analogous to the Péclet and Sharpening numbers, $\mathrm{Pe} = UL/\kappa = 100$, and $\mathrm{Sh} = (U\lambda)/\kappa = (\lambda/L)\mathrm{Pe} = 0.2$.

6.1. Static drop and Laplace's law

We consider a static drop of fluid with density ρ_1 in an infinite domain of fluid with density ρ_2 and measure the pressure across the interface. The pressure distribution should be smooth but oscillations are often observed in computations, potentially causing numerical instabilities. Figure 2 plots the pressure distribution for different non-dimensionalised values of λ when the grid Reynolds ($\mathrm{Re}_\Delta = c\Delta_x/\nu$) and grid capillary ($\mathrm{Ca}_\Delta = \rho_1 c\nu/\sigma$) numbers are 1 and 0.1, respectively. The left hand plot uses a resolution of 100×100 lattice points and a drop radius of $R = 25$ lattice units. When $\lambda = 0.1$ the sharpening is severe and causes oscillations in the pressure in the vicinity of the interface. Facetting of the interface was also observed. This behaviour is corrected as we increase λ: when $\lambda = 0.2$ the interface remains narrow with no oscillations but further increases smears the interface over more nodes. Doubling the resolution reduces the oscillations in the strict sharpening case ($\lambda = 0.1$) with pressure overshoots less than 5×10^{-5}. The source of the oscillations is suspected to be the on-lattice discretisation of gradient terms. More accurate representations of these terms is an option that is worthy of further research.

For illustration, Figure 3 plots the pressure distribution across the interface of a drop when the grid capillary number is increased by an order of magnitude to $\mathrm{Ca}_\Delta = 1$. All other parameters are unchanged. With a

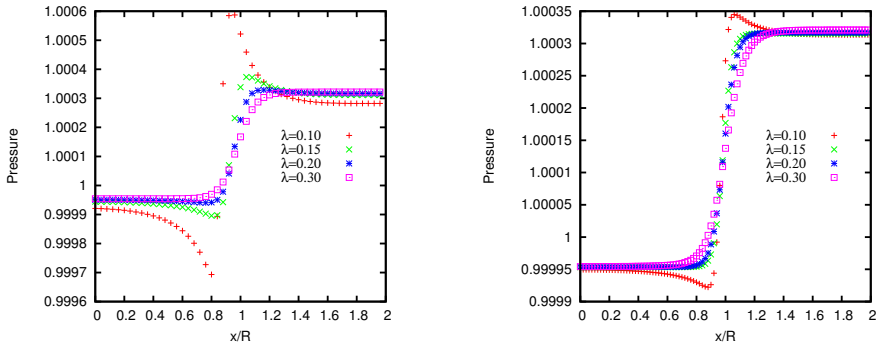

Figure 2: Pressure distribution across the interface of a static drop for different λ when the grid capillary number is $\mathrm{Ca}_\Delta = 0.1$ on a 100×100 grid (left) and a 200×200 grid.

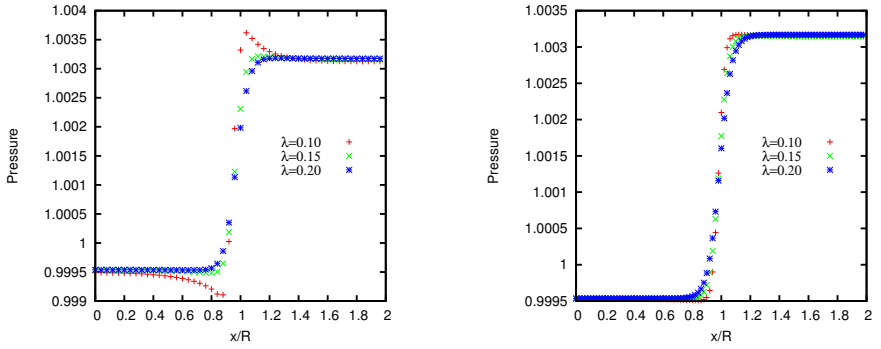

Figure 3: Pressure distribution across the interface of a static drop for different λ when the grid capillary number is $\mathrm{Ca}_\Delta = 1$ on a 100×100 grid (left) and a 200×200 grid.

resolution of 100×100 some small overshoot is observed in the pressure in the vicinity of the interface but the interface is very narrow. These small oscillations are quashed if we allow the interface to be a little more diffuse. Doubling the resolution removes all oscillations, even for very sharp interfaces with $\lambda = 0.1$.

Laplace's law states that

$$P_{in} - P_{out} = \frac{\sigma}{R}, \tag{57}$$

where P_{in} and P_{out} are the pressures inside and outside of a drop, respectively, and R is the radius of the drop. The surface tension, σ, is input

Ca_Δ	λ	Error_{100}	Error_{200}
0.01	0.1	0.2525	0.0090
	0.15	0.2540	0.0090
	0.2	0.0315	0.0090
0.1	0.1	0.1170	0.0055
	0.15	0.0190	0.0050
	0.2	0.0244	0.0090
1	0.1	0.0097	0.0019
	0.15	0.0061	0.0053
	0.2	0.0097	0.0091

Table 1: Comparison of surface tension measurements for different values of non-dimensionalised surface tension parameter σ and sharpening parameter λ on two grids.

directly into this one-fluid lattice Boltzmann model and thus the right hand side of Laplace's law (57) is known exactly and we measure the pressure difference. The pressure inside the drop was measured at its centre (centre of the domain) and the pressure outside was taken $(1/8)^{\text{th}}$ along each side. The error is calculated as the relative error between the exact and computed surface tension,

$$\mathrm{Error}_n = \frac{|\Delta P_{\text{exact}} - \Delta P_{\text{computed}}|}{\Delta P_{\text{exact}}},$$

where ΔP_{exact} and $\Delta P_{\text{computed}}$ and the right and left hand sides of equation (57), respectively, and the subscript n denotes the number of grid points on a side. The results are shown in Table 1. Except for the when $\mathrm{Ca}_\Delta = 0.1$ and $\lambda = 0.1$ on the 100×100 grid (which is when the largest oscillations were observed and the drop experienced facetting), the order of the relative error is never larger than 10^{-2} on the coarse grid and 10^{-3} on the finer grid. The errors are larger for more diffuse and overly sharp interfaces.

6.2. Layered Poiseuille flow

We compute the flow of layers of two fluids in an infinitely long channel of width $2H$. The flow is driven by a constant pressure gradient, imposed here via the body force $\mathbf{F} = (0, G)$. The force is scaled so that the maximum velocity in the flow is 1. The density of each fluid is constant and the flow is unidirectional so that $\mathbf{u} = (u_x(y), 0)$. The no-slip condition is imposed with the moment-based method and the constraints $u_x = u_y = 0$ and $\Pi_{xx} = P$ on

the plates [49, 50]. A brief overview of the moment-based method is given in Appendix B. Note that P on the plate is computed from the velocity conditions and known distributions, and the conditions on the moments have to be translated into conditions on "barred" functions [43]. A similar approach is used to impose conditions on the interface capturing equation, *i.e* ϕ, on the plates [51] and we note that the moment-based methodology has previously been used to compute multiphase flow and contact angles at boundaries [52]. To account for the rapid change in viscosity across the interface we use calculate the relaxation time in each phase according to the rule [53].

$$\mu = \begin{cases} \mu_1, & \phi \geq 0.5, \\ \mu_2, & \phi < 0.5. \end{cases}$$

When there are two layers of equal width the analytical solution is

$$u_x(y) = \begin{cases} \frac{GH^2}{2\mu_1}\left(-\left(\frac{y}{H}\right)^2 + \frac{y}{H}\left(\frac{\mu_1-\mu_2}{\mu_1+\mu_2}\right) + \left(\frac{2\mu_1}{\mu_1+\mu_2}\right)\right) & -H \leq y < 0 \\ \frac{GH^2}{2\mu_2}\left(-\left(\frac{y}{H}\right)^2 + \frac{y}{H}\left(\frac{\mu_1-\mu_2}{\mu_1+\mu_2}\right) + \left(\frac{2\mu_2}{\mu_1+\mu_2}\right)\right) & 0 \leq y \leq H \end{cases} \tag{58}$$

Figure 4 plots the analytical and computed velocity profiles when the densities of the fluid are equal but the kinematic viscosity ratio is $\nu_1/\nu_2 = 10$ and $\nu_1/\nu_2 = 1000$, where $\nu_n = \mu_n/\rho_n = \tau_n/3$. The surface tension parameter is set so that the capillary number is $Ca = \frac{U\mu_1}{\sigma} = 1$, where U is the maximum velocity, but tests with Ca ranging from 0.1 to 1000 showed no discernible difference, as should be expected. The velocity u is scaled by $c = \Delta x/\Delta t$ so that $u_{\max} = 0.1$. Results on two grids are shown: 1×129 and 1×257 grid points. While there is some numerical error at the interface the results are generally in excellent agreement, even for a very high viscosity ratio.

Next we consider two layer Poiseuille flow where the fluids have equal kinematic viscosities but different densities. Figure 5 plots the analytical and computed velocity profiles when the kinematic viscosities of the fluids are equal but the density ratios are $\rho_2/\rho_1 = 10$ and $\rho_2/\rho_1 = 1000$. The results are generally in excellent agreement, even for a very high density ratios, as confirmed by Figure 7, which plots the relative L_2 error on different grid sizes. Overall second order convergence is observed.

Figure 7 plots the relative L_2 error norm

$$E_2 = \sqrt{\frac{\sum_y \left(u_x(y) - u_{LBM}\right)^2}{\sum_y \left(u_x(y)\right)^2}},$$

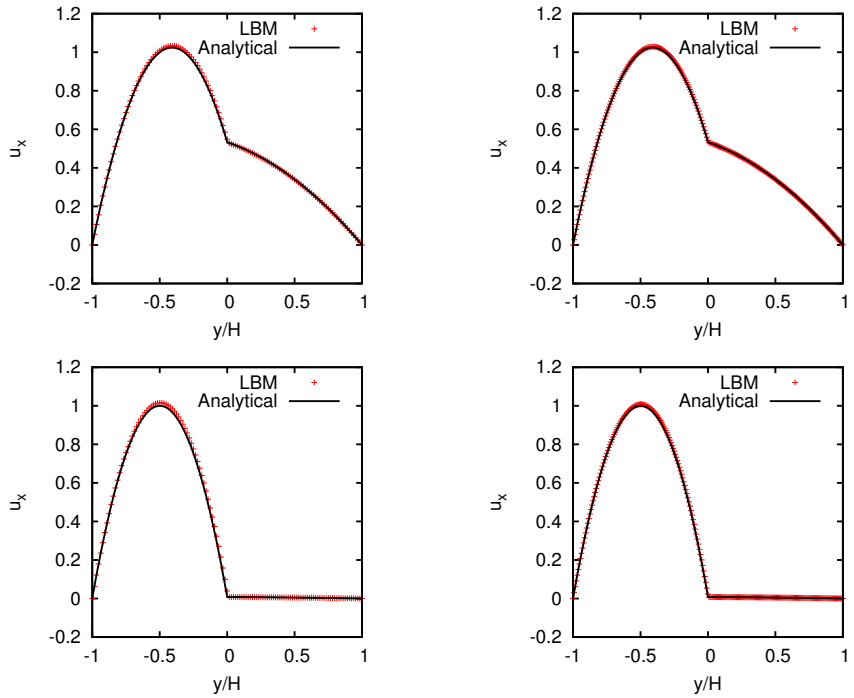

Figure 4: LBM computed and analytical velocity profile of two layer Poiseuille flow with equal densities and kinematic viscosity ratio $\nu_1/\nu_2 = 10$ (top) and $\nu_1/\nu_2 = 1000$ (bottom). The results on the left used a 1×129 grid and on the right a a 1×257 grid.

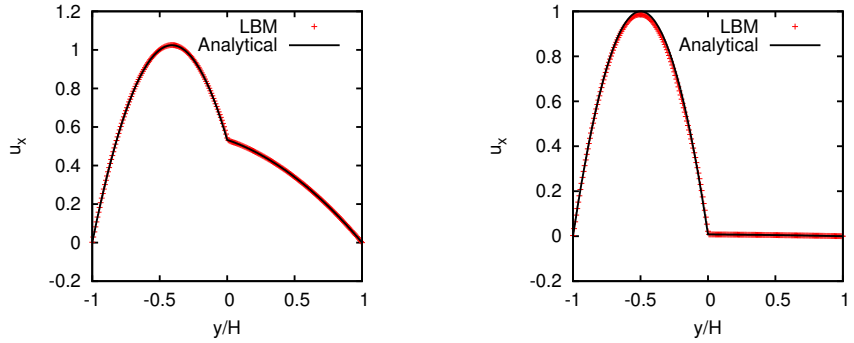

Figure 5: LBM computed and analytical velocity profile of two layer Poiseuille flow with equal kinematic viscosities and density ratios $\rho_2/\rho_1 = 10$ (left) and $\rho_2/\rho_1 = 1000$ on a 1×257 grid.

where u_{LBM} is the computed solution and $u(y)$ is given by equation (58), for different viscosity and density ratios on different size grids. The grid spacing $\Delta x = 1/(m-1)$, where m is the number of grid points in the channel width. It is seen that second order convergence is achieved when the kinematic viscosities are equal but the dynamic viscosities are different. When the kinematic viscosities of the fluids are different, overall second order convergence is observed for the smaller viscosity ratios, but with the rate reducing to almost first order for large grid size and ratios. We suspect that the slower convergence rate with large viscosity ratios is due to $\tau_f = \tau_f(\phi)$ varying considerably across the interface: there will be numerical errors due to the discretisation of gradients of ϕ, and τ_f appears inside divergence terms on the right hand side of equation (32). The error reduces to the order $\mathcal{O}(10^{-12})$ when the density and viscosity ratios are unity on a 1×3 grid, and the convergence rate for other parameter regimes is independent of the capillary number. Thus, and considering also that the flow is incompressible and unidirectional in each phase, we argue that the source of error is due to gradients in the material parameters across a transition region of finite width, noting that the analytical solution assumes an interface of zero thickness. The errors seen here with very large density and viscosity contrasts are still small and compare favourable with other schemes [53, 21, 54].

Figure 8 plots the analytical and numerical (LBM) solution of three layered Poiseuille flow when the dynamic viscosity of one fluid is 1000 times larger then the other. In the left hand plot the the inner fluid has the larger dynamic viscosity and in the right the outer fluid has the larger viscosity. The convergence of result with mesh refinement are shown in Figure 6. As in the two-layer flow, very good agreement with, and convergence to, analytical solutions are observed.

6.3. Rayleigh-Taylor instability

A fluid with density ρ_1 and dynamic viscosity μ_1 sits on top of a fluid with density $\rho_2 < \rho_1$ and viscosity μ_2 inside a domain of size $[0, L] \times [-2L, 2L]$. Solid horizontal no-slip boundaries are placed at the top and bottom of a horizontally periodic domain. Here $\mathrm{Ma} = \sqrt{3}/25$. Linear stability theory says that an interface perturbed to have the form $A\cos(kx)$ is unstable when the wavenumber is less than the critical wavenumber $k_c = (g(\rho_2 - \rho_1)/\sigma)^{1/2}$ [55]. In this case, gravity will allow the denser fluid to penetrate the other, causing rapid interfacial deformations known as the Rayleigh-Taylor instability. Here, and for comparison with benchmark simulations, the interface between the

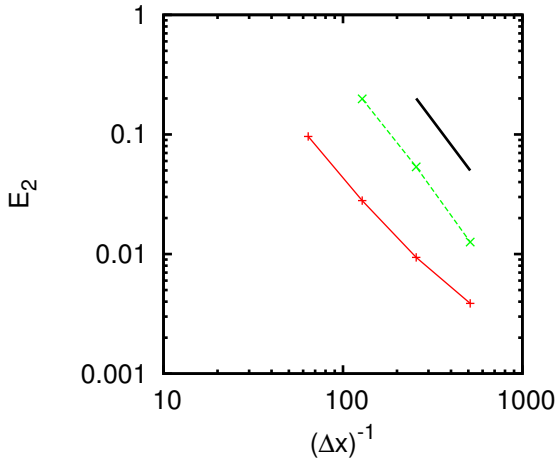

Figure 6: Relative L_2 errors of computed velocity profiles of three layer Poiseuille flow when $\mu_2/\mu_1 = 10$ (red) and $\mu_2/\mu_1 = 1000$ (green). The black line has slope 2.

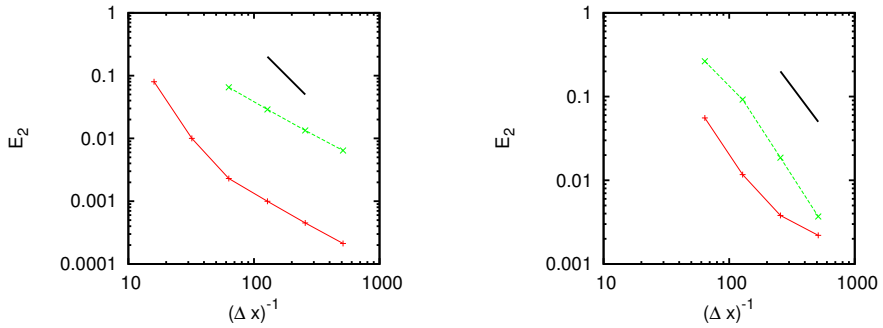

Figure 7: Relative errors of computed velocity profiles of two layer Poiseuille flow. Left: equal densities and $\nu_1/\nu_2 = 10$ (red); $\nu_1/\nu_2 = 1000$ (green). Right: equal kinematic viscosities and $\rho_2/\rho_1 = 10$ (red); $\rho_2/\rho_1 = 1000$ (green). Black line has slope 2.

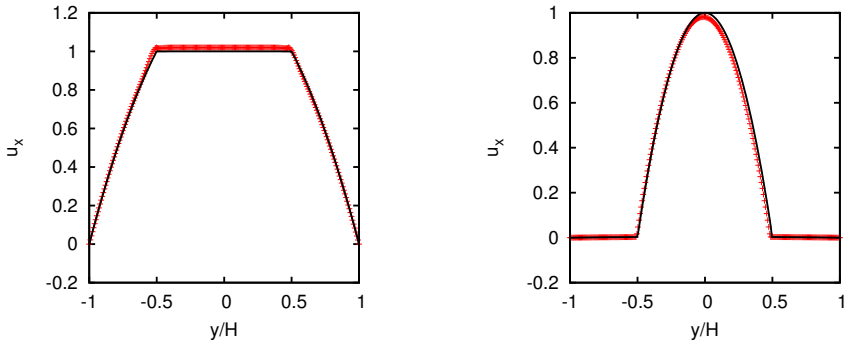

Figure 8: LBM computed (red points) and analytical velocity profile of three layer Poiseuille flow where the inner fluid has dynamic viscosity μ_1 and the outer μ_2. Left: $\mu_1/\mu_2 = 0.001$; Right: $\mu_1/\mu_2 = 1000$. The grid size is 1×257 and $\Delta t/\Delta x = 0.1$.

two fluids is perturbed and located at $y = 0.1L\cos(2\pi x/L)$. The Reynolds number is defined to be $\mathrm{Re} = \rho_1 U L/\mu_1$ and the characteristic velocity of the flow is determined by gravity, g, such that $U = |\sqrt{gL}|$. The density ratio is given by the Atwood number, $\mathrm{At} = (\rho_1 - \rho_2)/(\rho_1 + \rho_2)$, and the dynamic viscosities of the fluids are equal. In all simulations we set $\mathrm{Re} = 2048$ and $\mathrm{At} = 0.5$. We used a computational domain of size 257×1025 so that the grid spacing was $\Delta x = 1/256$ and we set the timestep according to $\Delta t/\Delta x = 0.04$ (meaning that $U = 0.04$ in lattice units). No-slip conditions were applied using the moment-based approach [50] and no flux conditions on the phase field [51].

Figure 9 plots on the top row the density at different moments in (non-dimensional) time, T, when there is no surface tension ($\sigma = 0$). The results are in qualitative agreement with benchmark simulations [7], showing the spikes of denser fluid and the rise of bubbles of lower density. The interface remains narrow in this and all simulations, typically containing no more than three grid points. For quantitative comparisons we plot in Figure 10 the position and speed of the interface and compare them with the data of Wang *et al.* [56], He *et al.* [7], and (where available) Nourgaliev *et al.* [57]. An excellent agreement is observed.

The middle row of Figure 9 shows the density contours when the capillary number $\mathrm{Ca} = 0.1$, so that surface tension forces dominate viscous forces. All other parameters are unchanged. We notice that surface tension has damped the secondary Kelvin-Helmholtz type instabilities at interfaces. No vortices

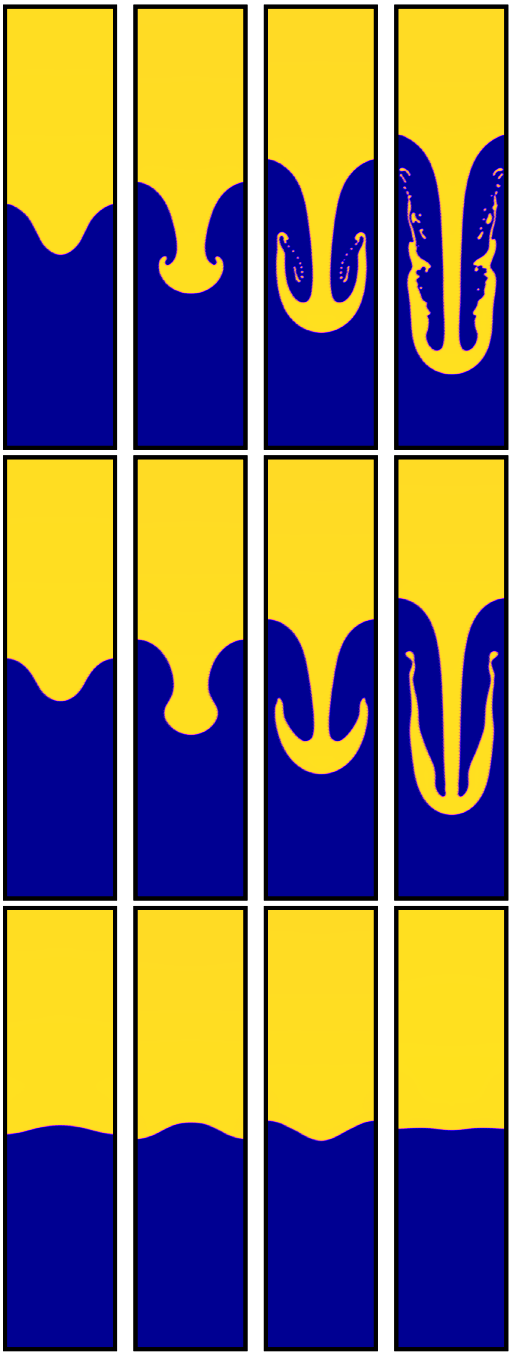

Figure 9: Density contours showing the Rayleigh-Taylor instability at different times when Re = 2048 and At = 0.5. Top row: No surface tension. Middle row: Ca = 0.1. Bottom row: Ca = 0.01. From left to right: $T = 1, 2, 3, 4$.

are formed or detached from the interface when Ca = 0.1, as anticipated [58]. If we reduce the capillary number further to Ca = 0.01 then surface tension is strong enough to stabilise the flow ($k > k_c$). That is, the heavier fluid does not penetrate into the lighter and the interface oscillates about its unperturbed state, $y = 0$, as shown on the bottom row of Figure 9.

6.4. Single bubble rise

A bubble of fluid with density ρ_1 and dynamic viscosity μ_1 is immersed in a fluid with density ρ_2 and dynamic viscosity μ_2, where $\rho_1 > \rho_2$. The domain size is $[0, 1] \times [0, 2]$ and the bubble is centred at (0.5,0.5) with radius $R = 0.25$. No-slip walls are places at $y = 0$ and $y = 2$, and free slip conditions at $x = 0$ and $x = 1$ using the moment-based approach [45]. The flow is characterised by the Reynolds and Bond numbers, which are given in terms of the diameter of the bubble and gravity:

$$\mathrm{Re} = \frac{\rho_1 \sqrt{g} (2R)^{3/2}}{\mu_1}; \quad \mathrm{Bo} = \frac{4\rho_1 g R^2}{\sigma}$$

and we measure the centre of mass, rise velocity, and circularity of the drop:

$$\mathbf{X}_c = \frac{\int_{\Omega_2} \mathbf{x}}{\int_{\Omega_2} 1}; \quad \mathbf{U}_c = \frac{\int_{\Omega_2 1} \mathbf{u}}{\int_{\Omega_2}}; \quad \epsilon = \frac{2\pi R}{P_{\mathrm{bubble}}},$$

where Ω_2 is the region occupied by the bubble and P_{bubble} is the perimeter of the bubble.

We first simulate the flow with Re = 35, Bo = 10, and $\rho_1/\rho_2 = \mu_1/\mu_2 = 10$. This has become known as "case 1" for the well-used benchmark test in multiphase CFD community [59, 60, 56]. The radius of the bubble has 50 lattice points and $\mathrm{Ma} = \sqrt{3}/1000$. The rise of the bubble up to non-dimensional time $T = 3$ is shown in Figure 11 and is in excellent qualitative agreement with benchmark simulations [59]. The centre of mass, rise velocity, and circularity are plotted in Figure 12 and compared with the benchmark data of Hysing *et al.* [59] from the *FreeLIFE* finite element level set solver. An excellent quantitative agreement is observed. The largest disagreement is in the circularity, but we note that this is still small and not unexpected when comparing a sharp interface level set approach with a method with diffuse (even if narrow) interfaces [61]. All multiphase LBMs have a distributed transition region. In addition, we show in Table 2 data for comparison with an advanced colour gradient LBM of Rothman-Keller type with the Reis and

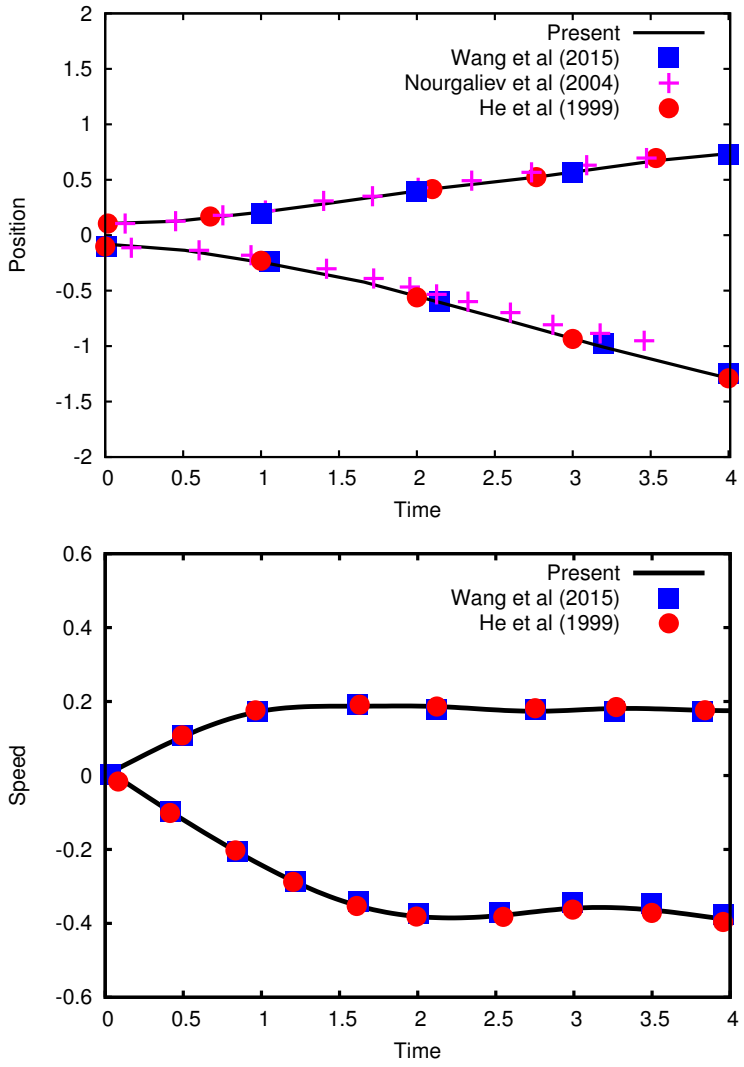

Figure 10: Comparison of interface position and velocity in the Rayleigh-Taylor instability test when $\mathrm{Re} = 2048$ and $\mathrm{At} = 0.5$.

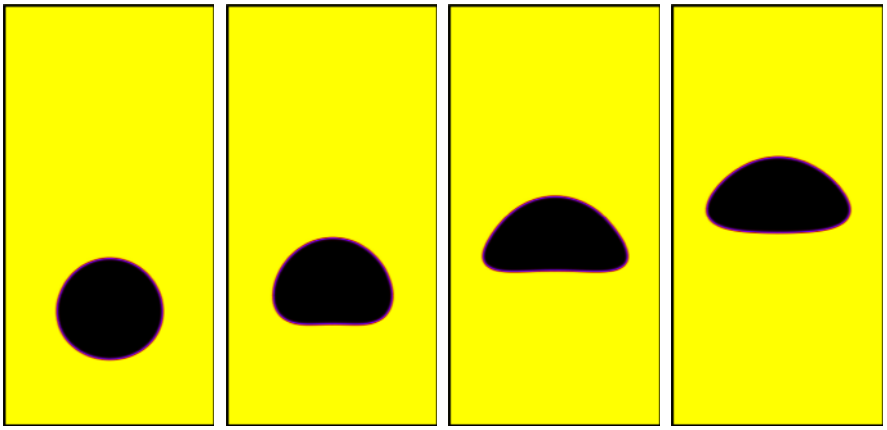

Figure 11: Density contours showing a single bubble rising in a denser fluid when Re = 35, Bo = 10, and $\rho_1/\rho_2 = \mu_1/\mu_2 = 10$. From left to right: $T = 0.5, 1, 2, 3$.

Phillips modification [16] and additional stability and performance enhancements of Leclaire *et al.* [62]. The table shows the minimum circularity, the time the minimum circularity occurred, the maximum rise velocity and the time of its occurrence, and the vertical coordinate of the centre of mass at $T = 3$. Three different meshes are used: with 20, 40, and 80 grid points in the initial radius. These correspond to the spatial resolution used in Leclaire *et al.* [62]. We note that results were also presented for a bubble radius of 10 grid points ($\Delta x = 1/40$) in [62]. We could not obtain results on such a coarse mesh without adjusting the sharpening parameters or the tolerance for computing $|\nabla\phi|$ in the numerator of $\mathbf{n}$ (but could if we allowed for wider interfaces), so for consistency we do not present those results. Data from the three finest resolutions used in the *FreeLife* and the *TP2D* level set finite element solvers, and the finite element arbitrary Lagrangian-Eulerian (ALE) solver *MooNMD*, found in [59] are also shown and once again we note the encouraging agreement using our simple model. We remark that we could obtain results with a Mach number an order of magnitude larger, but with a slight deterioration in results in comparison with other solvers. Similar data for diffuse interface models can be found in [61].

Finally, we compute the more challenging "case 2" bubble rise benchmark test, which sets Re = 35, Bo = 125, $\rho_1/\rho_2 = 1000$, and $\mu_1/\mu_2 = 100$. We could not obtain numerically stable results on very coarse grids so we used a spatial resolution of 100 grid points in a radius. We also needed to make the

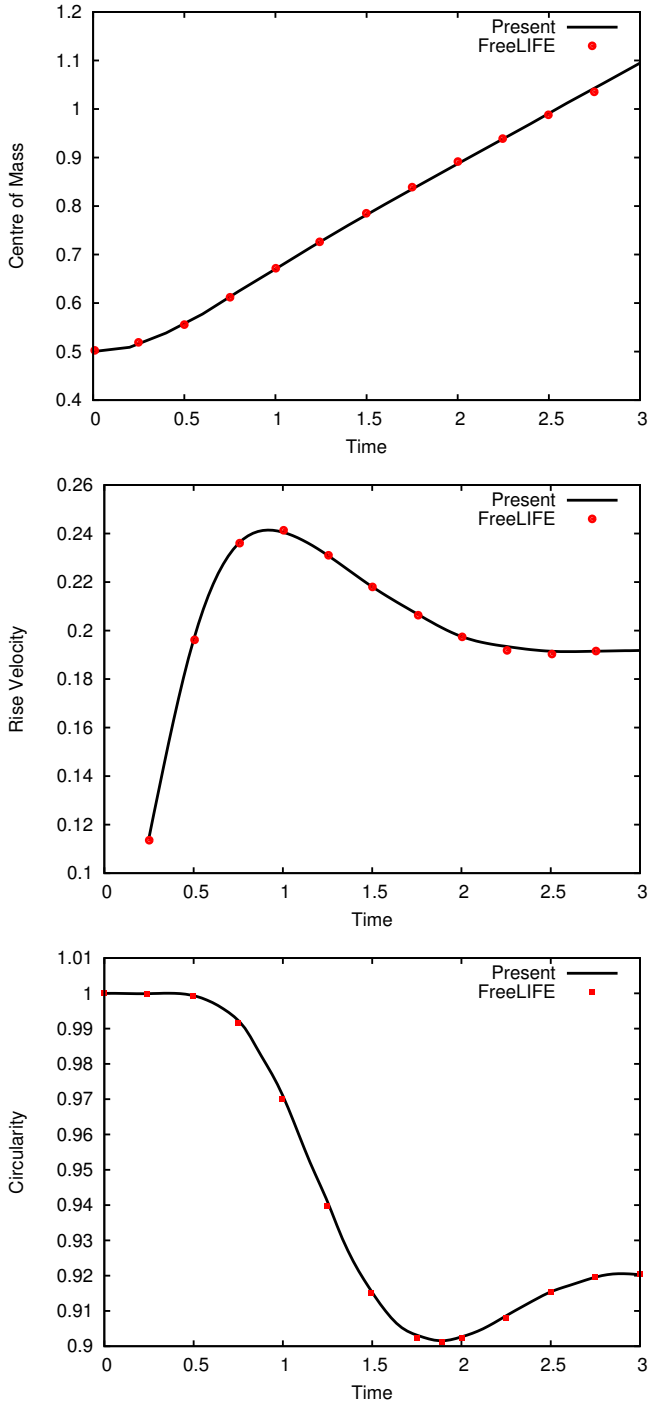

Figure 12: Plot of centre of mass, rise velocity, and circularity of a bubble in a denser fluid as a function of time when Re = 35, Bo = 10, and $\rho_1/\rho_2 = \mu_1/\mu_2 = 10$. Results from the FreeLIFE finite element software are also shown [59].

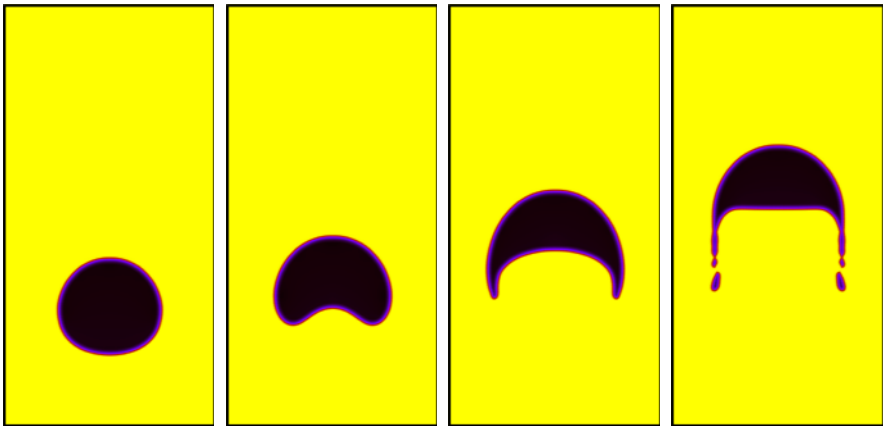

Figure 13: Density contours showing a single bubble rising in a denser fluid when Re = 35, Bo = 125, $\rho_1/\rho_2 = 1000$, and $\mu_1/\mu_2 = 100$. From left to right: $T = 0.5, 1, 2, 3$.

interface more diffuse than in "case 1" and it what follows we set Pe=10 and Sh=0.07. This is a famously difficult test and results of different solvers vary slightly, as shown in Hysing *et al.* [59], Wang *et al.* [56], and Aland and Voigt [61]. We plot in Figure 13 the rise of the bubble up to non-dimensional time $T = 3$ and observe a very good qualitative agreement with the literature [59]. Narrow filaments are predicted at $T = 3$. Fine grid sharp interface models suggest that there should not be any filaments [59] while diffuse interface models compute somewhat wider filaments [61]. Our model appears to capture the satellite bubbles trailing behind the main bubble - something computed by fine grid sharp interface models [59] but not classical diffuse interface models [61]. Figure 14 plots the centre of mass and the rise velocity as a function of non-dimensional time and compares them with the output of the *FreeLIFE* finite element level set software [59]. We do not compute the circularity because of the known discrepancy due to the filaments and satellites. An excellent agreement for the centre of mass is observed. There are some differences in the rise velocity but overall agreement is good (and we note that sharp interface and diffuse interface models compute different solutions [59, 61]). Thus we argue that while our results hint at areas for further development they also confirm the validity and potential of our raw model for computing multiphase flows in the presence of surface tension.

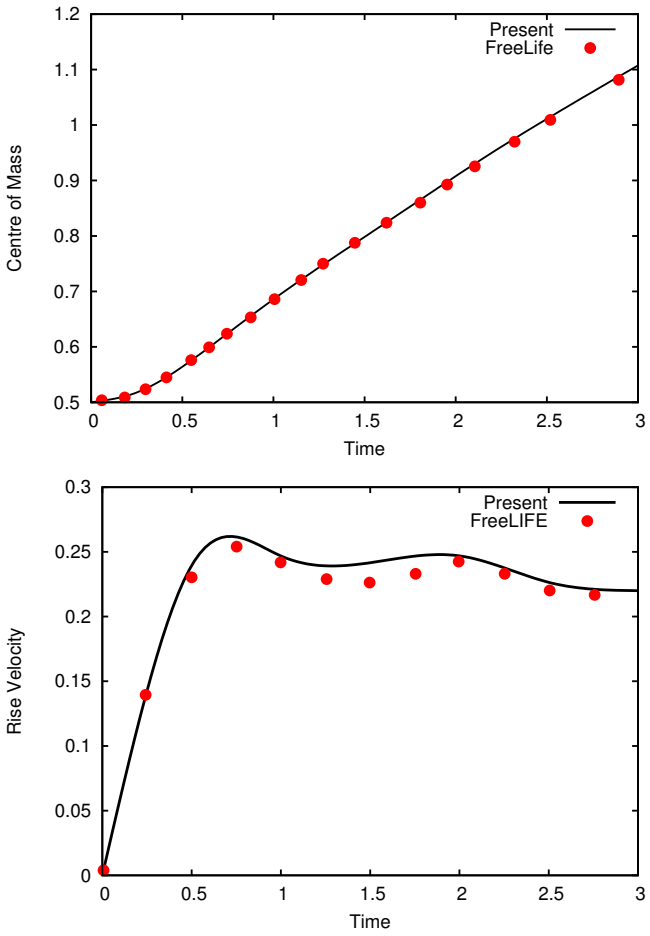

Figure 14: Plot of centre of mass (left) and rise velocity of a bubble in a denser fluid as a function of time when Re = 35, Bo = 125, $\rho_1/\rho_2 = 1000$ and $\mu_1/\mu_2 = 100$. Results from the FreeLIFE finite element software are also shown [59].

7. Conclusion

We have presented a new lattice Boltzmann method for computing solutions to the Navier-Stokes equations with the conservative form of the surface tension forces. In this model the surface tension is an independent parameter that can be set precisely *a priori*. High density and viscosity contrasts are achievable, while maintaining narrow boundaries between fluids. Since capillary effects are represented as the divergence of a tensor, they are incorporated naturally into the LBM momentum flux tensor and computed efficiently by the algorithm. No additional finite difference approximations are required for computing the divergence and the only non-local approximations required are for the unit normal to the interface, which are first order.

This approach involves two lattice Boltzmann equations: one for the hydrodynamics and another capturing interfaces. The capturing algorithm advects and sharpens the scalar field that distinguishes between fluids, allowing for narrow but finite transition widths. Thus interfaces are diffuse, rather than completely sharp, but are only distributed over a small number of lattice sites - typically 3 or 4 grid points. Indeed, the model is inspired by both diffuse interface lattice Boltzmann models for variable density flows in a "whole domain" formulation and colour gradient/continuous surface force lattice Boltzmann models for representing interfacial phenomena over hydrodynamic lengthscales.

The modelling errors in this LBM are consistent within the order of lattice Boltzmann and are negligible at small Mach numbers. Different formulations of the surface tension force may reduce these errors further, but this is a topic for later research. There are inevitable numerical errors in the approximation of the normal to the interface. In this work we have used only a very simple and primitive on-grid differencing scheme and have not considered compact stencils [10]. Similarly, we have used the simplest stencil for the interface capturing LBM - a 5 point lattice with a linear equilibrium function. The interface delta function, δ_s, has also been approximated quite primitively. Larger or more sophisticated differencing and lattices, and other forms of δ_s, may improve numerical accuracy and stability further, but this has not been investigated. Furthermore, alternative interface capturing algorithms could be coupled to the LBM hydrodynamic solver. The algebraic sharpening model of Reis and Dellar [30] may be advantageous for some problems, or the hydrodynamic LBM could be coupled to level set or artificial compression

algorithm, for example.

There is much scope for future research and development. As well as the suggestions above, the precise or optimal choice of sharpening and diffusion parameters (λ and κ) should be investigated. We know that the width of the transition region is a balance between sharpening and diffusion, but also that over sharpening ($\lambda \to 0$) and minimising diffusion ($\kappa \to 0$) can cause instabilities. An ad-hoc choice, albeit based on experience, of $0.1 \leq \mathrm{Sh} \leq 0.2$ with $\mathrm{Pe} = 100$ has allowed for stable computations with narrow interfaces in all but the most difficult tests, but a study of the interplay between the parameters and a theoretical rule would be very beneficial. One may also consider optimising the collision operator and we note that the basic model presented here can be used with any collision operator. Similarly, different forms of the forcing term could also be considered [63, 64]. Sophisticated multiphase CFD techniques might use flux limiters or mass redistribution steps to filter undershirts/overshoots and oscillations, or a Helmholtz smoother to enhance performance [12]. Similar methods could be used to the present lattice Boltzmann scheme to improve the "raw" model. The extension to three dimensions is natural and practical flows may benefit from non-uniform mesh refinement techniques or more sophisticated initialisations.

We have validated the model against analytical solutions and benchmark simulations. Agreement has been excellent over a range of parameter values, even for flows which are challenging for numerical methods. The lattice Boltzmann model presented here may be an attractive numerical tool for computing multiphase flow, particularly when surface tension effects are significant or in complex domains, because it incorporates surface tension conveniently and retains many of the computational advantages of the LBM methodology: simplicity, efficiency, and accuracy.

Acknowledgements

The author would link to thank the anonymous reviewers for helping to improve this article. This research forms part of the activities of the UK Consortium on Mesoscale Engineering Science (UKCOMES) under EPSRC grant no. EP/R029598/1

Appendix A. Summary of the algorithm

The discrete velocity Boltzmann equation (8), and its TRT form (45), with equilibria (23) and source terms (12,30) has embedded within its mo-

ments the multiphase Navier-Stokes equations (1,2). Equation (8) is solved numerically using the second order in time algorithm (48). The one-fluid formation couples the Navier-Stokes equations to an interface capturing equation, given here by equation (35). Equation (35) is embedded in the moments of the discrete velocity Boltzmann equation (36) with equilibria (38), which is solved numerically by (53). The structure of the one-fluid lattice Boltzmann algorithm that computes solutions to equations (1,2,3) is, after initialisation of $\overline{f}_i$ and $\overline{g}_i$ and ignoring boundaries:

1. compute $\phi = \sum_i \overline{g}_i$, $\rho = \rho_1\phi + \rho_2(1-\phi)$, and approximate δ_s (equation (56) used here), $\mathbf{n} = \nabla\phi/|\nabla\phi|$, and $\nabla\rho$ (scheme (55) used here for simplicity)
2. compute P and $\mathbf{u}$ from equations (49) and (50)
3. compute the equilibria for f_i (equations (43,44)) and g_i (equations (38,52))
4. collide (relax) and stream $\overline{f}_i$ (equation (48)) and $\overline{g}_i$ (equation (53))
5. repeat

The TRT collision procedure was used for both $\overline{f}_i$ and $\overline{g}_i$ but other collision operators could been used. The collision operator affects the numerics but does not change the model. For a single relaxation time (BGK) implementation one would simply set $\tau_f^+ = \tau_f^-$ and $\tau_g^+ = \tau_g-$. For a more general multiple relaxation time (MRT) collision operator, one could follow Dellar [2], for example. Implementation would involve computing moments, relaxing them to their equilibria (redefined to include any forces, similar to equations (43,44) here), and reconstructing the post-collisional $\overline{f}_i$ as a function of the post collisional moments (see [51, 65] for an outline algorithm).

Appendix B. Summary of moment-based boundary conditions

We impose boundary conditions upon moments of the lattice Boltzmann equations and then translate these into conditions on the unknown (incoming) f_i or $\overline{f}_i$ [49]. There are restrictions on the choice of moments: at a straight boundary aligned with grid points each moment contains one of three linear combinations of the unknown f_i, as shown in Table B.3. In this table $\mathbf{R} = \sum_i f_i \mathbf{c}_i\mathbf{c}_i\mathbf{c}_i\mathbf{c}_i$ and the subscripts N and T on the moments refer to the Cartesian coordinates normal and tangential to the boundary, respectively. The notation f_n denotes the lattice Boltzmann distribution with particle velocity in the same direction as the inward pointing unit normal,

n, to the boundary, f_{n+t} is the function with velocity in the direction of $n+t$, where t is the positive unit tangent to the boundary, and similarly for f_{n-t}. For example, at a boundary at the north of the computational domain, $n = (0, -1)$ and $t = (1, 0)$, so $f_n = f_4$, $f_{n+t} = f_8$, and $f_{n-t} = f_7$.

Now one imposes a boundary condition on one moment from each row of Table B.3 and solves for the unknown f_i. However, the second order discretisation discussed in Section 5 is in terms of $\overline{f}_i$, not f_i, so one first translates the boundary condition on the physical moments into conditions on "barred" moments using equation (47), and then solve for the incoming $\overline{f}_i$.

References

[1] X. He, L.-S. Luo, Theory of the lattice Boltzmann method: From the Boltzmann equation to the lattice Boltzmann equation, Phys. Rev. E 56 (1997) 6811–6817. doi:10.1103/PhysRevE.56.6811.

[2] P. J. Dellar, Incompressible limits of lattice Boltzmann equations using multiple relaxation times, J. Comput. Phys 190 (2) (2003) 351 – 370. doi:10.1016/S0021-9991(03)00279-1.

[3] B. Zhao, C. W. MacMinn, B. K. Primkulov, Y. Chen, A. J. Valocchi, J. Zhao, Q. Kang, K. Bruning, J. E. McClure, C. T. Miller, A. Fakhari, D. Bolster, T. Hiller, M. Brinkmann, L. Cueto-Felgueroso, D. A. Cogswell, R. Verma, M. Prodanović, J. Maes, S. Geiger, M. Vassvik, A. Hansen, E. Segre, R. Holtzman, Z. Yang, C. Yuan, B. Chareyre, R. Juanes, Comprehensive comparison of pore-scale models for multiphase flow in porous media, Proc. Natl. Acad. Sci. U.S.A. 116 (28) (2019) 13799–13806. doi:10.1073/pnas.1901619116.

[4] H. Liu, A. J. Valocchi, C. Werth, Q. Kang, M. Oostrom, Pore-scale simulation of liquid CO2 displacement of water using a two-phase lattice Boltzmann model, Adv. Water Resour. 73 (2014) 144 – 158. doi:10.1016/j.advwatres.2014.07.010.

[5] X. Shan, H. Chen, Lattice Boltzmann model for simulating flows with multiple phases and components, Phys. Rev. E 47 (1993) 1815–1819. doi:10.1103/PhysRevE.47.1815.

[6] M. R. Swift, W. R. Osborn, J. M. Yeomans, Lattice Boltzmann simulation of nonideal fluids, Phys. Rev. Lett. 75 (1995) 830–833. doi:10.1103/PhysRevLett.75.830.

[7] X. He, S. Chen, R. Zhang, A lattice Boltzmann scheme for incompressible multiphase flow and its application in simulation of Rayleigh-Taylor instability, J. Comput. Phys 152 (2) (1999) 642 – 663. doi:10.1006/jcph.1999.6257.

[8] A. Wagner, The origin of spurious velocities in lattice Boltzmann, Int. J. Mod. Phys B 17 (01n02) (2003) 193–196. doi:10.1142/S0217979203017448.

[9] T. Lee, C.-L. Lin, A stable discretization of the lattice Boltzmann equation for simulation of incompressible two-phase flows at high density ratio, J. Comput. Phys 206 (1) (2005) 16 – 47. doi:https://doi.org/10.1016/j.jcp.2004.12.001.

[10] T. Lee, P. F. Fischer, Eliminating parasitic currents in the lattice Boltzmann equation method for nonideal gases, Phys. Rev. E 74 (2006) 046709. doi:10.1103/PhysRevE.74.046709.

[11] A. Fakhari, M. Geier, T. Lee, A mass-conserving lattice Boltzmann method with dynamic grid refinement for immiscible two-phase flows, J. Comput. Phys 315 (2016) 434 – 457. doi:10.1016/j.jcp.2016.03.058.

[12] P.-H. Chiu, Y.-T. Lin, A conservative phase field method for solving incompressible two-phase flows, J. Comput. Phys 230 (2011) 185 – 204. doi:10.1016/j.jcp.2010.09.021.

[13] A. K. Gunstensen, D. H. Rothman, Lattice Boltzmann studies of immiscible two-phase flow through porous media, J. Geophys. Res. Solid Earth 98 (B4) (1993) 6431–6441. doi:10.1029/92JB02660.

[14] D. Grunau, S. Chen, K. Eggert, A lattice Boltzmann model for multiphase fluid flows, Phys Fluids 5 (10) (1993) 2557–2562. doi:10.1063/1.858769.

[15] D. Rothman, J. Keller, Immiscible cellular-automaton fluids, J. Stat. Phys. 52 (1988) 1119 – 1127. doi:10.1007/BF01019743.

[16] T. Reis, T. N. Phillips, Lattice Boltzmann model for simulating immiscible two-phase flows, J. Phys A 40 (14) (2007) 4033–4053. doi:10.1088/1751-8113/40/14/018.

[17] R. Scardovelli, S. Zaleski, Direct numerical simulation of free-surface and interfacial flow, Ann. Rev. Fluid Mech. 31 (1999) 567–603. doi:10.1146/annurev.fluid.31.1.567.

[18] H. Liu, A. J. Valocchi, Q. Kang, Three-dimensional lattice Boltzmann model for immiscible two-phase flow simulations, Phys. Rev. E 85 (2012) 046309. doi:10.1103/PhysRevE.85.046309.

[19] S. Leclaire, M. Reggio, J.-Y. Trèpanier, Isotropic color gradient for simulating very high-density ratios with a two-phase flow lattice Boltzmann model, Comput. Fluids 48 (2011) 98 – 112. doi:10.1016/j.compfluid.2011.04.001.

[20] S. Leclaire, A. Parmigiani, O. Malaspinas, B. Chopard, J. Latt, Generalized three-dimensional lattice Boltzmann color-gradient method for immiscible two-phase pore-scale imbibition and drainage in porous media, Phys. Rev. E 95 (2017) 033306. doi:10.1103/PhysRevE.95.033306.

[21] Z. X. Wen, Q. Li, Y. Yu, K. H. Luo, Improved three-dimensional color-gradient lattice Boltzmann model for immiscible two-phase flows, Phys. Rev. E 100 (2019) 023301. doi:10.1103/PhysRevE.100.023301.

[22] H. Wang, Y. Fu, Y. Wang, L. Yan, Y. Cheng, Three-dimensional lattice Boltzmann simulation of janus droplet formation in Y-shaped co-flowing microchannel, Chem. Eng. Sci. 225 (2020) 115819. doi:10.1016/j.ces.2020.115819.

[23] I. Halliday, S. P. Thompson, C. M. Care, Macroscopic surface tension in a lattice Bhatnagar-Gross-Krook model of two immiscible fluids, Phys. Rev. E 57 (1998) 514–523. doi:10.1103/PhysRevE.57.514.

[24] M. Latva-Kokko, D. H. Rothman, Static contact angle in lattice Boltzmann models of immiscible fluids, Phys. Rev. E 72 (2005) 046701. doi:10.1103/PhysRevE.72.046701.

[25] I. Halliday, A. P. Hollis, C. M. Care, Lattice Boltzmann algorithm for continuum multicomponent flow, Phys. Rev. E 76 (2007) 026708. doi:10.1103/PhysRevE.76.026708.

[26] S. V. Lishchuk, C. M. Care, I. Halliday, Lattice Boltzmann algorithm for surface tension with greatly reduced microcurrents, Phys. Rev. E 67 (2003) 036701. doi:10.1103/PhysRevE.67.036701.

[27] U. D'ortona, D. Salin, M. Cieplak, R. B. Rybka, J. R. Banavar, Two-color nonlinear Boltzmann cellular automata: Surface tension and wetting, Phys. Rev. E 51 (1995) 3718–3728. doi:10.1103/PhysRevE.51.3718.

[28] J. Spendlove, X. Xu, T. Schenkel, M. Seaton, I. Halliday, Chromodynamic multi-component lattice Boltzmann equation scheme for axial symmetry, J. Phys A: Math. and Theor.l 53 (2020) 145001. doi:10.1088/1751-8121/ab777f.

[29] J. Brackbill, D. Kothe, C. Zemach, A continuum method for modeling surface tension, J. Comp. Phys 100 (1992) 335 – 354. doi:https://doi.org/10.1016/0021-9991(92)90240-Y.

[30] T. Reis, P. Dellar, A volume-preserving sharpening approach for the propagation of sharp phase boundaries in multiphase lattice Boltzmann simulations, Comput. Fluids 46 (2011) 417 – 421. doi:10.1016/j.compfluid.2010.12.005.

[31] R. Leveque, H. Yee, A study of numerical methods for hyperbolic conservation laws with stiff source terms, J. Cop. Phys 86 (1990) 187 – 210. doi:10.1016/0021-9991(90)90097-K.

[32] Y. Sun, C. Beckermman, Sharp interface tracking using the phase-field equation, J. Comp. Phys 220 (2007) 626 – 653. doi:10.1016/j.jcp.2006.05.025.

[33] R. Folch, J. Casademunt, A. Hernández-Machado, L. Ramírez-Piscina, Phase-field model for Hele-Shaw flows with arbitrary viscosity contrast. i. Theoretical approach, Phys. Rev. E 60 (1999) 1724–1733. doi:10.1103/PhysRevE.60.1724.

[34] W. Bao, S. Jin, The random projection method for hyperbolic conservation laws with stiff reaction terms, J, Comp. Phys 163 (2000) 216 – 248. doi:10.1006/jcph.2000.6572.

[35] T. Reis, A conservative interface sharpening lattice Boltzmann model, SIAM J. Sci. Comput. 40 (2018) B1495–B1516. doi:10.1137/18M1184928.

[36] T. Reis, A multiphase lattice Boltzmann model for sharp interfaces, Presented at the Discrete Simulation of Fluid Dynamics conference, Fargo, USA (2011).

[37] T. Reis, Pinning and facetting in lattice Boltzmann simulations, URL: https://www.slideshare.net/TimReis2/workshop-presentations-lbworkshopreis (2010).

[38] E. Olsson, G. Kreiss, S. Zahedi, A conservative level set method for two phase flow ii, J. Comp. Phys 225 (2007) 785 – 807. doi:10.1016/j.jcp.2006.12.027.

[39] M. Geier, A. Fakhari, T. Lee, Conservative phase-field lattice Boltzmann model for interface tracking equation, Phys. Rev. E 91 (2015) 063309. doi:10.1103/PhysRevE.91.063309.

[40] P. J. Dellar, Lattice kinetic schemes for magnetohydrodynamics, J. of Comp. Phys 179 (2002) 95 – 126. doi:10.1006/jcph.2002.7044.

[41] L.-S. Luo, Unified theory of lattice Boltzmann models for nonideal gases, Phys. Rev. Lett. 81 (1998) 1618–1621. doi:10.1103/PhysRevLett.81.1618.
URL `https://link.aps.org/doi/10.1103/PhysRevLett.81.1618`

[42] D. d'Humiéres, I. Ginzburg, Viscosity independent numerical errors for lattice Boltzmann models: From recurrence equations to magic collision numbers, Comput. Math. with Appl. 58 (2009) 823 – 840. doi:10.1016/j.camwa.2009.02.008.

[43] T. Reis, On the lattice Boltzmann deviatoric stress: Analysis, boundary conditions, and optimal relaxation times, SIAM J. Sci. Comput. 42 (2) (2020) B397?B424.

[44] X. He, S. Chen, G. D. Doolen, A novel thermal model for the lattice Boltzmann method in incompressible limit, J. Comp. Phys 146 (1998) 282 – 300. doi:10.1006/jcph.1998.6057.

[45] S. Mohammed, D. I. Graham, T. Reis, Modeling the effects of slip on dipole-wall collision problems using a lattice Boltzmann equation method, Phys. Fluids 32 (2020) 025104. doi:10.1063/1.5131865.

[46] K. E. Teigen, P. Song, G. Lowengrub, A. Voigt, A diffuse-interface method for two-phase flows with soluble surfactants, J. Comp. Phys 230 (2011) 375–393. doi:https://doi.org/10.1016/j.jcp.2010.09.020.

[47] H. G. Lee, J. Kim, Regularized Dirac delta functions for phase field models, In. J. Num, Meth. Eng. 91 (2012) 269–288. doi:https://doi.org/10.1002/nme.4262.

[48] I. Ginzburg, D. d'Humiéres, A. Kuzmin, Optimal stability of advection-diffusion lattice Boltzmann models with two relaxation times for positive/negative equilibrium, J. Stat. Phys 139 (2010) 1090?1143. doi:10.1007/s10955-010-9969-9.

[49] S. Bennett, A lattice Boltzmann model for diffusion of binary gas mixtures, Ph.D. thesis, University of Cambridge, Department of Engineering (2010).

[50] S. Mohammed, D. Graham, T. Reis, Assessing moment-based boundary conditions for the lattice Boltzmann equation: A study of dipole-wall collisions, Comput. Fluids 176 (2018) 79 – 96. doi:10.1016/j.compfluid.2018.08.025.

[51] R. Allen, T. Reis, Moment-based boundary conditions for lattice Boltzmann simulations of natural convection in cavities, Prog. Comput. Fluid Dy. 16 (2016) 216–231. doi:10.1504/PCFD.2016.077296.

[52] A. Hantsch, T. Reis, U. Gross, Moment method boundary conditions for multiphase lattice Boltzmann simulations with partially-wetted walls, J. Comput. Multiphase Flow. 7 (2015) 1–14. doi:10.1260/1757-482X.7.1.1.

[53] X. Yuan, Z. Chai, H. Wang, B. Shi, A generalized lattice Boltzmann model for fluid flow system and its application in two-phase flows, Comput. Math. with Appl. 79 (2020) 1759 – 1780. doi:10.1016/j.camwa.2019.10.007.

[54] G. Thömes, J. Becker, M. Junk, A. K. Vaikuntam, D. Kehrwald, A. Klar, K. Steiner, A. Wiegmann, Lattice Boltzmann method for immiscible multiphase flow simulations using the level set method, J. Comp. Phys 228 (2009) 1139–1156. doi:https://doi.org/10.1016/j.jcp.2008.10.032.

[55] D. Livescu, Compressibility effects on the Rayleigh-Taylor instability growth between immiscible fluids, Physics of Fluids 16 (1) (2004) 118–127. doi:10.1063/1.1630800.

[56] Y. Wang, C. Shu, Y. C. Shao, J. Wu, X. D. Niu, A mass-conserved diffuse interface method and its application for incompressible multiphase flows with large density ratio, J. Comp. Phys. 290 (2015) 336 – 351. doi:https://doi.org/10.1016/j.jcp.2015.03.005.

[57] R. R. Nourgaliev, T. N. Dinh, T. G. Theofanous, A pseudocompressibility method for the simulation of incompressible multiphase flows, Int. J. Multiphase Flow 30 (2004) 901–937. doi:https://doi.org/10.1016/j.ijmultiphaseflow.2004.03.010.

[58] S. Yakovenko, The effect of density difference and surface tension on the development of Rayleigh-Taylor instability of an interface between fluid media, Fluid Dynamics. 49 (2014) 748–760. doi:10.1134/S0015462814060064.

[59] S. Hysing, S. Turek, D. Kuzmin, N. Parolini, E. Burman, S. Ganesan, L. Tobiska, Quantitative benchmark computations of two-dimensional bubble dynamics, Int. J. Num. Meth. Fluids 60 (11) (2009) 1259–1288. doi:https://doi.org/10.1002/fld.1934.

[60] B. S. Hosseini, S. Turek, M. Möller, C. Palmes, Isogeometric analysis of the navier-stokes-cahn-hilliard equations with application to incompressible two-phase flows, J. Comp. Phys. 348 (2017) 171 – 194. doi:https://doi.org/10.1016/j.jcp.2017.07.029.

[61] S. Aland, A. Voigt, Benchmark computations of diffuse interface models for two-dimensional bubble dynamics, Int. J. Num. Meth. Fluids 69 (2011) 747–761. doi:https://doi.org/10.1002/fld.2611.

[62] S. Leclaire, N. Pellerin, M. Reggio, J.-Y. Trèpander, A multiphase lattice Boltzmann method for simulating immiscible liquid-

liquid interface dynamics, Appl Math. Model 40 (2016) 6376 – 6394. doi:10.1016/j.apm.2016.01.049.

[63] A. A. Mohamad, A. Kuzmin, A critical evaluation of force term in lattice Boltzmann method, natural convection problem, Int. J. Heat Mass Trans. 53 (2010) 990–996. doi:https://doi.org/10.1016/j.ijheatmasstransfer.2009.11.014.

[64] G. Silva, Discrete effects on the forcing term for the lattice Boltzmann modeling of steady hydrodynamics, Comput. Fluids 203 (2020) 104537. doi:https://doi.org/10.1016/j.compfluid.2020.104537.

[65] T. Reis, Burnett order stress and spatially-dependent boundary conditions for the lattice Boltzmann method, Commun. Comp. Physics 27 (2019) 167–197. doi:10.4208/cicp.OA-2018-0229.

Variable	Method	Mesh 1	Mesh 2	Mesh 3
ϵ_{min}	Present	0.9332	0.9186	0.9023
	Leclaire [62]	0.9036	0.9021	0.9016
	FreeLife [59]	0.9021	0.9011	N/A
	TP2D [59]	0.9014	0.9014	0.9013
	MooNMD [59]	0.9018	0.9014	0.9013
$t\|_{\epsilon=\epsilon_{min}}$	Present	1.9430	1.9305	1.8990
	Leclaire [62]	1.9170	1.8979	1.9019
	FreeLife [59]	1.9125	1.8750	N/A
	TP2D [59]	1.8734	1.9070	1.9041
	MooNMD [59]	1.883	1.9013	1.9000
$U_{c,max}$	Present	0.1876	0.2451	0.2476
	Leclaire [62]	0.2428	0.2442	0.2429
	FreeLife [59]	0.2410	0.2421	N/A
	TP2D [59]	0.2418	0.2419	0.2417
	MooNMD [59]	0.2417	0.2417	0.2417
$t\|_{U_c=U_{c,max}}$	Present	0.9205	0.9475	0.9495
	Leclaire [62]	0.8825	0.9125	0.9117
	FreeLife [59]	0.9375	0.9313	N/A
	TP2D [59]	0.9375	0.9281	0.9213
	MooNMD [59]	0.9236	0.9214	0.9239
$y_c(T=3)$	Present	1.0809	1.0830	1.0827
	Leclaire [62]	1.0944	1.0883	1.0850
	FreeLife [59]	1.08175	1.0818	N/A
	TP2D [59]	1.0810	1.0812	1.0813
	MooNMD [59]	1.0823	1.0818	1.0817

Table 2: Measured outputs and comparisons for Case 1

Moments	Combination of unknowns
ρ, ρu_N, Π_{NN}	$f_n + f_{n+t} + f_{n-t}$
ρu_T, Π_{TN}, Q_{TNN}	$f_{n+t} - f_{n-t}$
Π_{TT}, Q_{TTN}, R_{TTNN}	$f_{n+t} + f_{n-t}$

Table B.3: Moment groups at a straight boundary